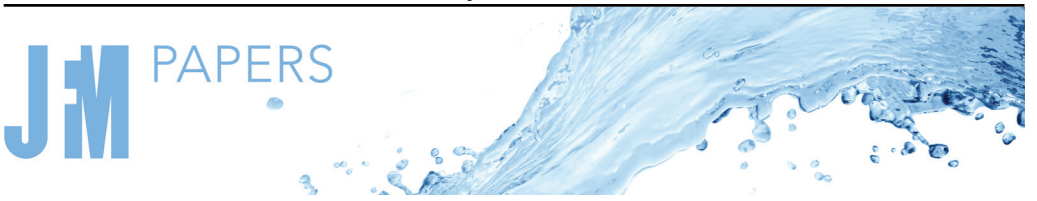
J. Fluid Mech. (2026), *vol.* 1026, A30, doi:10.1017/jfm.2025.11027



Convective and inertial Marangoni surfing

Saeed Jafari Kang[1], **Esmaeil Dehdashti**[1], **Jonathan P. Rothstein**[2] **and Hassan Masoud**[3]

[1]Department of Mechanical and Aerospace Engineering, Michigan Technological University, Houghton, MI 49931, USA

[2]Department of Mechanical and Industrial Engineering, University of Massachusetts, Amherst, MA 01003, USA

[3]Department of Mechanical Engineering, Clemson University, Clemson, SC 29634, USA

Corresponding author: Hassan Masoud, hmasoud@clemson.edu

(Received 2 May 2025; revised 19 November 2025; accepted 29 November 2025)

We study the surfing motion of an active particle along a planar interface, separating a semi-infinite layer of gas from a deep layer of liquid. The interface-trapped particle self-propels, thanks to an uneven distribution of surface tension in its immediate vicinity, which itself results from a non-uniform release of an active agent from the particle's surface. We use the reciprocal theorem in conjunction with singular perturbation expansions to calculate the leading-order contributions to the propulsion speed of the surfer due to the advective transport of mass and momentum when the Péclet and Reynolds numbers (denoted by Pe and Re, respectively) are small but finite. Assuming that the surface tension varies linearly with the concentration of the agent with a slope of negative α, we show, perhaps unexpectedly, that the normalised speed for a purely translating (but otherwise arbitrarily shaped) particle, independent of the agent discharge mechanism, can be expressed as $\mathscr{U} = 1 + \mathscr{A}(2Pe \ln Pe + Re \ln Re) + \mathscr{O}(Pe) + \mathscr{O}(Re)$, where the prefactor $\mathscr{A}$ is positive for negative α and *vice versa*. For reference, the self-propulsion speed of autophoretic Janus spheres varies with Pe as $\mathscr{U} = 1 + \mathscr{B}\,Pe + \cdots$, where $\mathscr{B}$ is positive when the mobility coefficient of the particle is negative and *vice versa*. Also, the speed of spherical squirmers changes with Re as $\mathscr{U} = 1 + \mathscr{C}\,Re + \mathscr{O}(Re)^2$, with $\mathscr{C}$ being positive for pushers and negative for pullers. Our asymptotic formula reveals that the speed of a Marangoni surfer is a non-monotonic function of the Péclet and Reynolds numbers, hinting at the existence of optimal values for both Pe and Re. The information contained within the multiplier $\mathscr{A}$ also offers guidance for customising the shape of the surfer, as well as the release rate and configuration of the agent, to enhance the self-surfing performance. Our general theoretical analysis is complemented by detailed numerical simulations for a representative spherical surfer. These simulations confirm our theoretical predictions and

© The Author(s), 2026. Published by Cambridge University Press. This is an Open Access article, distributed under the terms of the Creative Commons Attribution licence (https://creativecommons.org/licenses/by/4.0/), which permits unrestricted re-use, distribution and reproduction, provided the original article is properly cited.

https://doi.org/10.1017/jfm.2025.11027 Published online by Cambridge University Press

shed light on the effects of intermediate and large values of *Pe* and *Re* on the performance of Marangoni surfers.

Key words: interfacial flows (free surface), multiphase and particle-laden flows, propulsion

1. Introduction

The propulsion of floating objects due to auto-generated surface-tension gradients, also known as Marangoni surfing, stands as a fascinating phenomenon observed in the world of living organisms while also bearing promising potential for robotic applications. For example, in nature, this mode of locomotion is employed by water-walking insects for speedy movement in emergency situations (Linsenmair & Jander 1963; Andersen 1976; Schildknecht 1976; Bush & Hu 2006; Bush, Hu & Prakash 2007; Lang, Seifert & Dettner 2012) and by certain bacterial swarms for rapid interfacial migration toward nutrient-rich regions for further colonisation (Harshey 2003; Daniels *et al.* 2006; Angelini *et al.* 2009; Kearns 2010; Fauvart *et al.* 2012). In the realm of human-made systems, arguably, the most basic form of Marangoni surfing is realised in a camphor/soap boat, where the gradual dissolution of a camphor/soap piece attached to the back of a boat (representative of a floating object) creates a fore–aft surface-tension asymmetry (with associated Marangoni flows) that leads to the self-propulsion of the craft. Over the years, various adaptations of this rudimentary surfer concept have been developed, with sizes ranging from a few micrometres to more than ten centimetres (Kitahata *et al.* 2004; Su 2007; Bassik, Abebe & Gracias 2008; Soh, Bishop & Grzybowski 2008; Shibuya & Matsushita 2009; Nakata & Murakami 2010; Suematsu *et al.* 2010; Soh, Branicki & Grzybowski 2011; Jin *et al.* 2012; Li *et al.* 2012; Luo *et al.* 2012; Qiao *et al.* 2012; Sharma, Chang & Velev 2012; Zhao & Pumera 2012; Bansagi *et al.* 2013; Renney, Brewer & Mooibroek 2013; Zhang *et al.* 2013; Burton, Cheng & Bush 2014; Pimienta & Antoine 2014; Xiao, Jiang & Shi 2014; Maggi *et al.* 2015; Ooi *et al.* 2015; Satterwhite-Warden *et al.* 2015; Srinivasan *et al.* 2015; Girot *et al.* 2016; Liakos *et al.* 2016; Musin *et al.* 2016; Srivastava & Schmidt 2016; Wang *et al.* 2016; Frenkel *et al.* 2017; Koyano *et al.* 2017; Sharma *et al.* 2017; Zhang *et al.* 2017; Ivanov & Nikolov 2019; Löffler *et al.* 2019; Morohashi, Imai & Toyota 2019; Sur, Masoud & Rothstein 2019; Pena-Francesch, Giltinan & Sitti 2019; Dietrich *et al.* 2020; Sur *et al.* 2021). Notably, some of the more recent and sophisticated versions, such as the robots engineered by Kwak & Bae (2017), Kwak, Choi & Bae (2020), Kwak *et al.* (2021), Basualdo *et al.* (2021), Timm *et al.* (2021) and Bechard *et al.* (2023), have demonstrated capabilities applicable to a wide range of tasks, including environmental sensing and monitoring, microfluidic manipulation and self-assembly.

In order to drive continued progress in the development of advanced surfing robots powered by the Marangoni effect, it is imperative to establish a comprehensive understanding of Marangoni propulsion across a spectrum of operating conditions. Among the fundamental research conducted on this subject to date (Kitahata *et al.* 2004; Nagayama *et al.* 2004; Soh *et al.* 2008; Lauga & Davis 2012; Masoud & Shelley 2014; Masoud & Stone 2014; Würger 2014; Malgaretti, Popescu & Dietrich 2016; Vandadi, Jafari Kang & Masoud 2017; Domínguez & Popescu 2018; Boniface *et al.* 2019; Gidituri, Panchagnula & Pototsky 2019; Crowdy 2020, 2021; Jafari Kang *et al.* 2020; Boniface *et al.* 2021; Ender & Kierfeld 2021), the predominant focus of the theoretical efforts has been centred on cases characterised by negligible advective transport of mass (or heat) and momentum, where the Péclet and Reynolds numbers (represented by *Pe* and *Re*, respectively) approach zero. However, many practical scenarios do not conform to such

https://doi.org/10.1017/jfm.2025.11027 Published online by Cambridge University Press

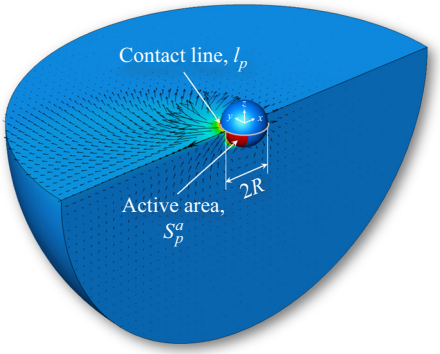


Figure 1. Schematic of a half-submerged spherical surfer located atop an (ideally) unbounded liquid layer. The active area of the surfer is coloured red, and the colour map and vector plots represent the concentration distribution and liquid velocity field in the vicinity of the surfer, respectively.

idealised conditions. Consequently, there is a need for further theoretical insights to inform the design of robots capable of efficiently navigating in these non-ideal regimes.

To address the aforementioned demand, we examine the Marangoni-driven motion of a chemically active particle along a flat liquid–gas interface. First, we use the reciprocal theorem to derive a generally valid formula relating the propulsion speed of the active surfer to surface and volume integrals involving, respectively, the concentration and velocity fields around it. We then employ the perturbation theory to evaluate those integrals in the limits of small Péclet and Reynolds numbers and show, to the leading order, how the speed of a purely translating surfer changes as a result of non-zero *Pe* and *Re*. Motivated by our theoretical findings, next, we consider a representative spherical surfer and study its propulsion behaviour over a broad span of *Pe* and *Re* values (well beyond the validity range of the theory) via detailed numerical simulations. The results of our calculations are presented in the form of performance regime maps that pinpoint optimal surfing scenarios. Below, we present our theoretical derivations (§ 2), followed by the description of our computational approach (§ 3). The outcomes of our investigation are discussed afterward (§ 4), and concluding remarks are given at the end (§ 5).

2. Problem statement and perturbation solution

2.1. *Assumptions and governing equations*

Consider the motion of a particle located at an interface between a semi-infinite layer of gas and an identical layer of liquid with density ϱ, viscosity μ and surface tension γ. The movement of the particle is caused by an asymmetric release of a chemical species, with diffusivity $\mathscr{D}$, from the particle's surface (see, e.g. figure 1). Our initial goal is to formulate a theoretical expression for the self-propulsion speed of the particle in the limits of small Péclet and Reynolds numbers. To reduce the complexity of the derivation, we assume that (i) the liquid–gas interface is flat, (ii) the effect of flow in the gas phase is negligible, (iii) the released chemical species is soluble in the bulk of the liquid layer, (iv) the liquid is at rest and contains no amount of the chemical species far from the particle, (v) the liquid is Newtonian with constant density and viscosity that are unaffected by the presence of the solute, (vi) the surface tension of the liquid varies linearly with the concentration of the chemical species, (vii) no velocity slip occurs on the wetted surface of the surfer due to tangential concentration gradients and (viii) the particle undergoes a pure translational motion along a straight line parallel to the interface.

https://doi.org/10.1017/jfm.2025.11027 Published online by Cambridge University Press

Let $\boldsymbol{r} = x\boldsymbol{e}_x + y\boldsymbol{e}_y + z\boldsymbol{e}_z$ be the position vector with $r = |\boldsymbol{r}|$ in the Cartesian coordinate system (x, y, z), with the unit vectors $\boldsymbol{e}_x$, $\boldsymbol{e}_y$ and $\boldsymbol{e}_z$ such that $\boldsymbol{e}_x$ is aligned with the propulsion direction of the surfer, $\boldsymbol{e}_z$ is normal to the interface pointing away from the liquid and the origin of the coordinates coincides with the geometrical centre of the three-phase contact line denoted by l_p (see figure 1). Also, let c, $\boldsymbol{u} = u_x\boldsymbol{e}_x + u_y\boldsymbol{e}_y + u_z\boldsymbol{e}_z$ and p, represent, respectively, the dimensionless, steady-state concentration field of the chemical species and the velocity and pressure fields of the liquid. With these definitions and the above-mentioned assumptions, the equations that govern the distributions of c, $\boldsymbol{u}$ and p in a coordinate system attached to the particle are (see, e.g. Masoud & Stone 2019, p. 37)

$$\nabla^2 c = Pe\,(\boldsymbol{u} - \mathscr{U}\boldsymbol{e}_x)\cdot\boldsymbol{\nabla} c, \tag{2.1a}$$

with the boundary conditions

$$\boldsymbol{n}\cdot\boldsymbol{\nabla} c = 0 \quad \text{for} \quad \boldsymbol{r}\in S_i, \tag{2.1b}$$

$$c \to 0 \quad \text{as} \quad r\to\infty, \tag{2.1c}$$

and

$$\boldsymbol{\nabla}\cdot\boldsymbol{\sigma} - Re(\boldsymbol{u} - \mathscr{U}\boldsymbol{e}_x)\cdot\boldsymbol{\nabla}\boldsymbol{u} = \nabla^2\boldsymbol{u} - \boldsymbol{\nabla} p - Re(\boldsymbol{u} - \mathscr{U}\boldsymbol{e}_x)\cdot\boldsymbol{\nabla}\boldsymbol{u} = \boldsymbol{0}, \tag{2.2a}$$

$$\boldsymbol{\nabla}\cdot\boldsymbol{u} = 0, \tag{2.2b}$$

with the boundary conditions

$$\boldsymbol{u} = \mathscr{U}\boldsymbol{e}_x \quad \text{for} \quad \boldsymbol{r}\in S_p, \tag{2.2c}$$

$$\boldsymbol{u} \to \boldsymbol{0} \quad \text{as} \quad r\to\infty, \tag{2.2d}$$

$$u_z = 0 \quad \text{and} \quad (\boldsymbol{I} - \boldsymbol{nn})\cdot(\boldsymbol{n}\cdot\boldsymbol{\sigma}) = -\left(\frac{\partial u_x}{\partial z}\boldsymbol{e}_x + \frac{\partial u_y}{\partial z}\boldsymbol{e}_y\right) = -\boldsymbol{\nabla}_{S_i}\gamma \quad \text{for} \quad \boldsymbol{r}\in S_i. \tag{2.2e}$$

Here, S_i, S_p, $\boldsymbol{\sigma} = -p\boldsymbol{I} + \mu[\boldsymbol{\nabla}\boldsymbol{u} + (\boldsymbol{\nabla}\boldsymbol{u})^T]$, $\boldsymbol{I}$, $\boldsymbol{n}$ and $\boldsymbol{\nabla}_{S_i}$ denote the liquid–gas interface, the wet surface of the surfer, the stress tensor, the identity tensor, the unit normal vector and the surface gradient operator taking effect along S_i, respectively. Also,

$$Pe = \frac{U^\star \ell}{\mathscr{D}}, \qquad Re = \frac{\varrho U^\star \ell}{\mu} \qquad \text{and} \qquad \mathscr{U} = \frac{\underset{\sim}{U}}{U^\star}, \tag{2.3}$$

where ℓ is the radius of the smallest sphere that encloses the surfer, $\underset{\sim}{\boldsymbol{U}} = \underset{\sim}{U}\boldsymbol{e}_x$ is the (dimensional) propulsion velocity of the surfer and $U^\star$ represents the value of $\underset{\sim}{U}$ in the absence of advective effects (i.e. when the concentration and flow fields are governed by diffusion and Stokes equations, respectively). Note that we intentionally refrained from specifying a boundary condition for c on S_p in order to avoid constraining the problem to a particular release mechanism.

2.2. *An integral formulation for the propulsion speed*

Consider the auxiliary problem of Stokes flow around the same surfer travelling with velocity $\underset{\sim}{U}_a = \underset{\sim}{U}_a\boldsymbol{e}_x$ (where $\underset{\sim}{U}_a = |\underset{\sim}{U}_a|$) when no surface-tension gradients (i.e. Marangoni stresses) are present. The (dimensionless) velocity and the stress fields, in this case, follow

$$\boldsymbol{\nabla}\cdot\boldsymbol{\sigma}_a = \nabla^2\boldsymbol{u}_a - \boldsymbol{\nabla} p_a = \boldsymbol{0}, \tag{2.4a}$$

$$\boldsymbol{\nabla}\cdot\boldsymbol{u}_a = 0, \tag{2.4b}$$

https://doi.org/10.1017/jfm.2025.11027 Published online by Cambridge University Press

with the boundary conditions

$$\boldsymbol{u}_a = \boldsymbol{e}_x \quad \text{for} \quad \boldsymbol{r} \in S_p, \tag{2.4c}$$

$$\boldsymbol{u}_a \to \boldsymbol{0} \quad \text{as} \quad r \to \infty, \tag{2.4d}$$

$$u_{a,z} = 0 \quad \text{and} \quad (\boldsymbol{I} - \boldsymbol{nn}) \cdot (\boldsymbol{n} \cdot \boldsymbol{\sigma}_a) = \boldsymbol{0} \quad \text{for} \quad \boldsymbol{r} \in S_i. \tag{2.4e}$$

According to Lamb's general solution of the Stokes equations (Lamb 1932, see also Brenner & Cox 1963), far from the surfer, $\boldsymbol{u}_a$ behaves as

$$\boldsymbol{u}_a = {}_{-1}\boldsymbol{u}_a + \mathscr{O}(r^{-2}), \tag{2.5}$$

where

$${}_{-1}\boldsymbol{u}_a = \frac{1}{4\pi r}\left(\boldsymbol{I} + \frac{\boldsymbol{rr}}{r^2}\right) \cdot F_a\, \boldsymbol{e}_x, \tag{2.6}$$

$$-F_a \boldsymbol{e}_x = \boldsymbol{F}_a = \int_{S_p} \boldsymbol{n} \cdot \boldsymbol{\sigma}_a \, \mathrm{d}S. \tag{2.7}$$

Next, apply the reciprocal theorem between the velocity–stress pairs $(\boldsymbol{u}, \boldsymbol{\sigma})$ and $(\boldsymbol{u}_a, \boldsymbol{\sigma}_a)$ (see, e.g. Masoud & Stone 2019, p. 14) to arrive at

$$\int_S \boldsymbol{n} \cdot \boldsymbol{\sigma} \cdot \boldsymbol{u}_a \, \mathrm{d}S - \int_S \boldsymbol{n} \cdot \boldsymbol{\sigma}_a \cdot \boldsymbol{u} \, \mathrm{d}S = Re \int_V (\mathscr{U}\boldsymbol{e}_x - \boldsymbol{u}) \cdot \boldsymbol{\nabla u} \cdot \boldsymbol{u}_a \, \mathrm{d}V, \tag{2.8a}$$

where V and $S = S_i + S_p + S_\infty$ represent the volume and outer surface of the entire liquid domain, respectively. The integrals over S_∞ (the bounding surfaces at very large distances) are zero since the velocities decay at least as fast as $1/r$. Hence, we have

$$\int_{S_i} \boldsymbol{n} \cdot \boldsymbol{\sigma} \cdot \boldsymbol{u}_a \, \mathrm{d}S + \int_{S_p} \boldsymbol{n} \cdot \boldsymbol{\sigma} \cdot \boldsymbol{u}_a \, \mathrm{d}S - \int_{S_i} \boldsymbol{n} \cdot \boldsymbol{\sigma}_a \cdot \boldsymbol{u} \, \mathrm{d}S$$
$$- \int_{S_p} \boldsymbol{n} \cdot \boldsymbol{\sigma}_a \cdot \boldsymbol{u} \, \mathrm{d}S = Re \int_V (\mathscr{U}\boldsymbol{e}_x - \boldsymbol{u}) \cdot \boldsymbol{\nabla u} \cdot \boldsymbol{u}_a \, \mathrm{d}V. \tag{2.8b}$$

From the force balance on the surfer and the boundary conditions described by (2.2c)–(2.2), (2.1b) and (2.1c), we infer

$$(\boldsymbol{n} \cdot \boldsymbol{\sigma} \cdot \boldsymbol{u}_a)\big|_{S_i} = -\boldsymbol{\nabla}_{S_i}\gamma \cdot \boldsymbol{u}_a|_{S_i}, \tag{2.9a}$$

$$\int_{S_p} \boldsymbol{n} \cdot \boldsymbol{\sigma} \cdot \boldsymbol{u}_a \, \mathrm{d}S = \int_{S_p} \boldsymbol{n} \cdot \boldsymbol{\sigma} \, \mathrm{d}S \cdot \boldsymbol{e}_x = -\int_{l_p} \gamma \boldsymbol{t} \, \mathrm{d}l \cdot \boldsymbol{e}_x = -\boldsymbol{F}_{st} \cdot \boldsymbol{e}_x = -F_{st}, \tag{2.9b}$$

$$\int_{S_i} \boldsymbol{n} \cdot \boldsymbol{\sigma}_a \cdot \boldsymbol{u} \, \mathrm{d}S = 0, \tag{2.9c}$$

$$\int_{S_p} \boldsymbol{n} \cdot \boldsymbol{\sigma}_a \cdot \boldsymbol{u} \, \mathrm{d}S = \int_{S_p} \boldsymbol{n} \cdot \boldsymbol{\sigma}_a \, \mathrm{d}S \cdot \mathscr{U}\boldsymbol{e}_x = -F_a \, \mathscr{U}, \tag{2.9d}$$

where $\boldsymbol{t}$ is the unit vector tangent to S_i and normal to l_p, and F_a is non-dimensionalised by $\mu U_a \ell$. Therefore, we can write

$$-F_{st} - \int_{S_i} \boldsymbol{\nabla}_{S_i}\gamma \cdot \boldsymbol{u}_a \, \mathrm{d}S + F_a \, \mathscr{U} = Re \int_V (\mathscr{U}\boldsymbol{e}_x - \boldsymbol{u}) \cdot \boldsymbol{\nabla u} \cdot \boldsymbol{u}_a \, \mathrm{d}V, \tag{2.10a}$$

which leads to

$$\mathscr{U} = \frac{F_{st}}{F_a} + \int_{S_i} \boldsymbol{\nabla}_{S_i}\gamma \cdot \left(\frac{\boldsymbol{u}_a}{F_a}\right) \mathrm{d}S + Re \int_V (\mathscr{U}\boldsymbol{e}_x - \boldsymbol{u}) \cdot \boldsymbol{\nabla u} \cdot \left(\frac{\boldsymbol{u}_a}{F_a}\right) \mathrm{d}V. \tag{2.10b}$$

https://doi.org/10.1017/jfm.2025.11027 Published online by Cambridge University Press

The above integral relation for the propulsion speed can be expressed alternatively as

$$\mathscr{U} = -\int_{S_i} (\gamma - \gamma_0)\, \boldsymbol{\nabla}_{S_i} \cdot \left(\frac{\boldsymbol{u}_a}{F_a}\right) \mathrm{d}S + Re\left[\int_V \boldsymbol{u} \cdot \boldsymbol{\nabla}\left(\frac{\boldsymbol{u}_a}{F_a}\right) \cdot \boldsymbol{u}\, \mathrm{d}V - \mathscr{U}\boldsymbol{e}_x \cdot \int_V \boldsymbol{\nabla}\left(\frac{\boldsymbol{u}_a}{F_a}\right) \cdot \boldsymbol{u}\, \mathrm{d}V\right], \tag{2.10c}$$

given that

$$\begin{aligned}(\mathscr{U}\boldsymbol{e}_x - \boldsymbol{u}) \cdot \boldsymbol{\nabla}\boldsymbol{u} \cdot \boldsymbol{u}_a &= \mathscr{U}\boldsymbol{e}_x \cdot \boldsymbol{\nabla}\boldsymbol{u} \cdot \boldsymbol{u}_a - \boldsymbol{u} \cdot \boldsymbol{\nabla}\boldsymbol{u} \cdot \boldsymbol{u}_a \\ &= \mathscr{U}\boldsymbol{e}_x \cdot [\boldsymbol{\nabla}\,(\boldsymbol{u} \cdot \boldsymbol{u}_a) - \boldsymbol{\nabla}\boldsymbol{u}_a \cdot \boldsymbol{u}] - \boldsymbol{\nabla} \cdot (\boldsymbol{u}\boldsymbol{u} \cdot \boldsymbol{u}_a) + \boldsymbol{u} \cdot \boldsymbol{\nabla}\boldsymbol{u}_a \cdot \boldsymbol{u},\end{aligned} \tag{2.11}$$

and that

$$\boldsymbol{\nabla}_{S_i}\gamma \cdot \boldsymbol{u}_a = \boldsymbol{\nabla}_{S_i} \cdot (\gamma \boldsymbol{u}_a) - \gamma\, \boldsymbol{\nabla}_{S_i} \cdot \boldsymbol{u}_a = \boldsymbol{\nabla}_{S_i} \cdot [(\gamma - \gamma_0)\boldsymbol{u}_a] - (\gamma - \gamma_0)\, \boldsymbol{\nabla}_{S_i} \cdot \boldsymbol{u}_a. \tag{2.12}$$

2.3. *Singular perturbation expansions of the velocity and concentration fields*

Suppose $Pe \ll 1$ and $Re \ll 1$, and let

$$\gamma = \gamma_0 - \frac{\alpha \dot{m}^\star}{2\pi\, \mathscr{D}\mu U^\star\, \ell}\, c, \tag{2.13}$$

where γ_0 is a non-dimensional constant and $\dot{m}^\star$ is the release rate of the chemical species when the concentration field is governed solely by diffusion. Here, γ and c are made dimensionless by $\mu U^\star$ and $\dot{m}^\star/2\pi\mathscr{D}\ell$, respectively. To evaluate (2.10*c*) in the limits of small Péclet and Reynolds numbers, we proceed with perturbation expansions of c and $\boldsymbol{u}$ in terms of Pe and Re. It is widely known that regular expansions fail to deliver satisfactory approximations due to the far-field behaviour of the concentration and velocity distributions in the purely diffusive and purely viscous limits. Therefore, we adopt the singular perturbation technique, which involves distinct expansions for regions in proximity to and distant from the particle, referred to as the inner and outer regions, respectively (see, e.g. Lagerstrom & Cole 1955; Kaplun 1957; Kaplun & Lagerstrom 1957; Proudman & Pearson 1957; Van Dyke 1964; Hinch 1991; Leal 2007). The inner and outer expansions are asymptotically matched in an intermediate region, where both of them are applicable. As demonstrated by Lovalenti & Brady (1993), these regional expansions can be merged (while carefully avoiding duplication of overlapping regions) to form approximations that remain uniformly valid across the domain V (see also Dehdashti & Masoud 2020). Following this approach, c and $\boldsymbol{u}$ can be expressed as

$$\begin{aligned}c = {} & \underbrace{c^{(0,0)}}_{\substack{\text{zeroth-order}\\ \text{solution}}} + \underbrace{Pe\, c^{(1,0)}}_{\substack{\text{First-order inner}\\ \text{approximation}}} + \underbrace{Pe\, \check{c}^{(1,0)}}_{\substack{\text{First-order outer}\\ \text{approximation}}} - \underbrace{\left(c_\infty^{(0,0)} + Pe\, c_\infty^{(1,0)}\right)}_{\text{Overlapping terms}} \\ & + \mathscr{O}\left(Pe^2 \ln Pe\right) + \mathscr{O}(Pe\, Re \ln Re),\end{aligned} \tag{2.14}$$

$$\begin{aligned}\boldsymbol{u} = {} & \underbrace{\boldsymbol{u}^{(0,0)}}_{\substack{\text{zeroth-order}\\ \text{solution}}} + \underbrace{Re \ln Re\, \boldsymbol{u}^{(0,1)} + Re\, \boldsymbol{u}^{(0,2)}}_{\substack{\text{First- and second-order}\\ \text{inner approximations}}} + \underbrace{Re\, \tilde{\boldsymbol{u}}^{(0,1)}}_{\substack{\text{First-order outer}\\ \text{approximation}}} \\ & - \underbrace{\left(\boldsymbol{u}_\infty^{(0,0)} + Re \ln Re\, \boldsymbol{u}_\infty^{(0,1)} + Re\, \boldsymbol{u}_\infty^{(0,2)}\right)}_{\text{Overlapping terms}} + \mathscr{O}\left(Re^2 \ln Re\right) + \mathscr{O}(Pe \ln Pe),\end{aligned} \tag{2.15}$$

https://doi.org/10.1017/jfm.2025.11027 Published online by Cambridge University Press

where the infinity subscript denotes the leading-order contributions to the corresponding terms in the limit that $r \to \infty$. Also, $\vee$ and $\sim$ overbars denote that the concentration and velocity fields, as well as the $\boldsymbol{\nabla}$ and ∇^2 operators in the following equations, are written in terms of the stretched (rescaled) position vectors $\check{\boldsymbol{r}} = Pe\,\boldsymbol{r}$ and $\tilde{\boldsymbol{r}} = Re\,\boldsymbol{r}$, respectively. Note that the coefficients of the expansion terms in (2.14) and (2.15) are not strictly required to be simple powers of the perturbation parameters (i.e. Re and Pe). Instead, they are determined by the boundary and matching conditions, as will become evident shortly.

2.3.1. *Zeroth- and first-order approximations for the concentration field*

Substituting the zeroth-order term along with the inner and outer expansions from (2.14) into (2.1) and equating like powers of Pe, we arrive at the following boundary value problems:

$$\nabla^2 c^{(0,0)} = 0, \tag{2.16a}$$

$$\boldsymbol{n} \cdot \boldsymbol{\nabla} c^{(0,0)} = 0 \quad \text{for} \quad \boldsymbol{r} \in S_i, \tag{2.16b}$$

$$c^{(0,0)} \to 0 \quad \text{as} \quad r \to \infty, \tag{2.16c}$$

$$\check{\boldsymbol{\nabla}}^2 \check{c}^{(1,0)} = -\boldsymbol{e}_x \cdot \check{\boldsymbol{\nabla}} \check{c}^{(1,0)}, \tag{2.17a}$$

$$\boldsymbol{n} \cdot \check{\boldsymbol{\nabla}} \check{c}^{(1,0)} = 0 \quad \text{for} \quad \check{\boldsymbol{r}} \in S_i, \tag{2.17b}$$

$$\check{c}^{(1,0)} \to 0 \quad \text{as} \quad \check{r} \to \infty, \tag{2.17c}$$

$$\nabla^2 c^{(1,0)} = \left(\boldsymbol{u}^{(0,0)} - \boldsymbol{e}_x\right) \cdot \boldsymbol{\nabla} c^{(0,0)}, \tag{2.18a}$$

$$\boldsymbol{n} \cdot \boldsymbol{\nabla} c^{(1,0)} = 0 \quad \text{for} \quad \boldsymbol{r} \in S_i, \tag{2.18b}$$

$$\lim_{r\to\infty} c^{(0,0)} + Pe \lim_{r\to\infty} c^{(1,0)} = Pe \lim_{\check{r}\to 0} \check{c}^{(1,0)}. \tag{2.18c}$$

Following Brenner (1963), the asymptotic solutions to (2.15)–(2.17) in the limits of $r \gg 1$ and $\check{r} \ll 1$ are given by

$$c^{(0,0)} = \frac{1}{r} + \mathscr{O}(r^{-2}), \tag{2.19}$$

$$c^{(1,0)} = -\frac{1}{2}\left(1 + \frac{x}{r}\right) + \mathscr{O}(r^{-1}), \tag{2.20}$$

$$\check{c}^{(1,0)} = \frac{1}{\check{r}} \exp\left[-\frac{1}{2}\left(\check{r} + \check{x}\right)\right] = \frac{1}{\check{r}} - \frac{1}{2}\left(1 + \frac{\check{x}}{\check{r}}\right) + \mathscr{O}(\check{r}). \tag{2.21}$$

A key parameter for assessing the propulsion efficiency of the surfer (defined either as the distance travelled per unit mass of 'fuel' released or as the speed achieved per unit rate of fuel consumed) is the total release rate of the chemical species, expressed as

$$\dot{m} = -\mathscr{D} \int_{S_p} \boldsymbol{n} \cdot \underset{\sim}{\nabla} \underset{\sim}{c}\, \mathrm{d}\tilde{S}, \tag{2.22}$$

where a tilde underbar indicates dimensional variables and operators. Adopting an approach akin to that of Brenner (1963) (see also Dehdashti & Masoud 2020), it can be shown that the Sherwood number (denoted by Sh), takes the form

$$Sh = Sh^\star + \frac{(Sh^\star)^2}{2} Pe + \mathscr{O}\left(Pe^2 \ln Pe\right) + \mathscr{O}(Pe\,Re \ln Re), \tag{2.23}$$

with

$$Sh = \frac{\dot{m}}{2\pi \mathscr{D} \ell \underset{\sim}{c}_s} \quad \text{and} \quad Sh^\star = \frac{\dot{m}^\star}{2\pi \mathscr{D} \ell \underset{\sim}{c}_s}, \tag{2.24}$$

https://doi.org/10.1017/jfm.2025.11027 Published online by Cambridge University Press

valid for the special case where the wet surface of the surfer is divided into an active region, S_p^a, maintained at a uniform (dimensional) concentration c_s, and an inactive region, S_p^{ia}, on which a no-flux condition ($\boldsymbol{n}\cdot\boldsymbol{\nabla}c=0$) is imposed (see, e.g. Masoud & Rothstein 2022).

2.3.2. *Zeroth- and first-order outer approximations for the velocity field*
Similarly, substituting the expansion (2.15) into the Navier–Stokes equations (2.2) and collecting terms of equal powers in Re yield the following governing equations for the leading-order inner and outer velocity fields:

$$\boldsymbol{\nabla}\cdot\boldsymbol{\sigma}^{(0,0)}=\nabla^2\boldsymbol{u}^{(0,0)}-\boldsymbol{\nabla}p^{(0,0)}=\boldsymbol{0}, \tag{2.25a}$$

$$\boldsymbol{\nabla}\cdot\boldsymbol{u}^{(0,0)}=0, \tag{2.25b}$$

$$\boldsymbol{u}^{(0,0)}=\boldsymbol{e}_x \quad \text{for} \quad \boldsymbol{r}\in S_p, \tag{2.25c}$$

$$\boldsymbol{u}^{(0,0)}\to\boldsymbol{0} \quad \text{as} \quad r\to\infty, \tag{2.25d}$$

$$u_z^{(0,0)}=0 \quad \text{and} \quad \left(\frac{\partial u_x^{(0,0)}}{\partial z}\boldsymbol{e}_x+\frac{\partial u_y^{(0,0)}}{\partial z}\boldsymbol{e}_y\right)=\boldsymbol{\nabla}_{S_i}\gamma^{(0,0)} \quad \text{for} \quad \boldsymbol{r}\in S_i, \tag{2.25e}$$

$$\tilde{\nabla}^2\tilde{\boldsymbol{u}}^{(0,1)}-\tilde{\boldsymbol{\nabla}}\tilde{p}^{(0,1)}+\boldsymbol{e}_x\cdot\tilde{\boldsymbol{\nabla}}\tilde{\boldsymbol{u}}^{(0,1)}=\boldsymbol{0}, \tag{2.26a}$$

$$\tilde{\boldsymbol{\nabla}}\cdot\tilde{\boldsymbol{u}}^{(0,1)}=0, \tag{2.26b}$$

$$\tilde{\boldsymbol{u}}^{(0,1)}\to\tilde{\boldsymbol{u}}^{(0,0)} \quad \text{as} \quad \tilde{r}\to 0, \tag{2.26c}$$

$$\tilde{\boldsymbol{u}}^{(0,1)}\to\boldsymbol{0} \quad \text{as} \quad \tilde{r}\to\infty, \tag{2.26d}$$

$$\tilde{u}_z^{(0,1)}=0 \quad \text{and} \quad \left(\frac{\partial\tilde{u}_x^{(0,1)}}{\partial\tilde{z}}\boldsymbol{e}_x+\frac{\partial\tilde{u}_y^{(0,1)}}{\partial\tilde{z}}\boldsymbol{e}_y\right)=\tilde{\boldsymbol{\nabla}}_{S_i}\tilde{\gamma}_\infty^{(0,0)} \quad \text{for} \quad \tilde{\boldsymbol{r}}\in S_i. \tag{2.26e}$$

Note that the boundary condition at the interface in (2.26) also ensures that

$$\lim_{r\to\infty}\boldsymbol{u}^{(0,0)}=Re\lim_{\tilde{r}\to 0}\boldsymbol{u}^{(0,1)}. \tag{2.27}$$

Let ${}_{-1}\boldsymbol{u}^{(0,0)}$ be the solution to (2.25) correct to $\mathscr{O}(r^{-1})$. This velocity field corresponds to the monopolar contribution of the zeroth-order concentration field, denoted henceforth by ${}_{-1}c^{(0,0)}=1/r$ (see (2.19)). As described below, ${}_{-1}\boldsymbol{u}^{(0,0)}$ can be calculated by applying the Fourier transform in the x–y plane.

We begin by taking the Fourier transform of ${}_{-1}c^{(0,0)}$:

$$\begin{aligned}\mathfrak{F}_{xy}\{{}_{-1}c^{(0,0)}\}={}_{-1}\widehat{c}^{(0,0)}&=\int_{-\infty}^{\infty}\int_{-\infty}^{\infty}\frac{\exp\left[-i\left(k_x x+k_y y\right)\right]}{\sqrt{x^2+y^2+z^2}}\,\mathrm{d}x\,\mathrm{d}y\\&=2\pi\int_0^{\infty}\frac{J_0(k\rho)}{\sqrt{\rho^2+z^2}}\,\rho\,\mathrm{d}\rho=2\pi\frac{\exp(kz)}{k},\end{aligned} \tag{2.28}$$

where $i^2=-1$, $k=|\boldsymbol{k}|$ with $\boldsymbol{k}=(k_x,k_y)$ being the in-plane wave vector, J_0 the zeroth-order Bessel function of the first kind and $\rho=\sqrt{x^2+y^2}$ (see Gradshteyn & Ryzhik 2007; Baddour 2011, 6.565-2). Note that $z<0$ in the liquid phase beneath the interface, as illustrated in figure 1. Combining the result from (2.28) with the derivation presented in the supplementary material of Masoud & Shelley (2014) for Marangoni-driven Stokes

https://doi.org/10.1017/jfm.2025.11027 Published online by Cambridge University Press

flow, we obtain

$$\mathfrak{F}_{xy}\Big\{{}_{-1}\boldsymbol{u}^{(0,0)}\Big\} = {}_{-1}\widehat{\boldsymbol{u}}^{(0,0)} = -\left(\frac{\alpha\dot{m}^{\star}}{\mathscr{D}\mu U^{\star}\ell}\right)\frac{\exp(kz)}{2}\left[\frac{i\boldsymbol{k}}{k^2}\,(1+kz)+z\,\boldsymbol{e}_z\right]. \tag{2.29}$$

Taking the inverse Fourier transform of (2.29), we then find (see again, Gradshteyn & Ryzhik 2007; Baddour 2011, 6.611-1,6.621-4)

$$\begin{aligned}
{}_{-1}\boldsymbol{u}^{(0,0)}\left(\frac{\alpha\dot{m}^{\star}}{4\pi\,\mathscr{D}\mu U^{\star}\ell}\right)^{-1} &= -2\pi\;\mathfrak{F}_{xy}^{-1}\left\{\exp(kz)\left[\frac{i\boldsymbol{k}}{k^2}\,(1+kz)+z\,\boldsymbol{e}_z\right]\right\}\\
&= -2\pi\;\nabla_{xy}\,\mathfrak{F}_{xy}^{-1}\left\{\exp(kz)\left(\frac{1+kz}{k^2}\right)\right\} - 2\pi\;\mathfrak{F}_{xy}^{-1}\{\exp(kz)z\}\,\boldsymbol{e}_z\\
&= -\nabla_{xy}\int_0^{\infty}\frac{\exp(kz)\,(1+kz)}{k^2}J_0(k\rho)\,k\,\mathrm{d}k - z\int_0^{\infty}\exp(kz)\;J_0(k\rho)\,k\,\mathrm{d}k\,\boldsymbol{e}_z\\
&= -\int_0^{\infty}\frac{\exp(kz)\,(1+kz)}{k^2}\nabla_{xy}J_0(k\rho)\,k\,\mathrm{d}k + \frac{z^2}{r^3}\,\boldsymbol{e}_z\\
&= \int_0^{\infty}\exp(kz)\,(1+kz)\;J_1(k\rho)\,\mathrm{d}k\,\boldsymbol{e}_{\rho} + \frac{z^2}{r^3}\boldsymbol{e}_z\\
&= \left[\frac{1}{\rho}\left(1+\frac{z}{r}\right)+\frac{\rho z}{r^3}\right]\boldsymbol{e}_{\rho} + \frac{z^2}{r^3}\,\boldsymbol{e}_z = \frac{1}{r}\left[(1+2\cos\theta)\,\boldsymbol{e}_r + \frac{\sin\theta\cos\theta}{1-\cos\theta}\boldsymbol{e}_{\theta}\right],
\end{aligned} \tag{2.30}$$

where

$$\nabla_{xy}J_0(k\rho) = \frac{\partial J_0(k\rho)}{\partial x}\boldsymbol{e}_x + \frac{\partial J_0(k\rho)}{\partial y}\boldsymbol{e}_y = \frac{\mathrm{d}J_0(k\rho)}{\mathrm{d}\rho}\boldsymbol{e}_{\rho} = -kJ_1(k\rho)\,\boldsymbol{e}_{\rho}, \tag{2.31}$$

and J_1 is the first-order Bessel function of the first kind. Here, we have expressed the velocity field in both cylindrical and spherical coordinate systems, (ρ, φ, z) and (r, θ, φ), respectively. The associated unit vectors $(\boldsymbol{e}_{\rho}, \boldsymbol{e}_{\varphi}, \boldsymbol{e}_z)$ and $(\boldsymbol{e}_r, \boldsymbol{e}_{\theta}, \boldsymbol{e}_{\varphi})$ are related to the Cartesian basis via

$$\boldsymbol{e}_{\rho} = \cos\varphi\,\boldsymbol{e}_x + \sin\varphi\,\boldsymbol{e}_y, \tag{2.32}$$
$$\boldsymbol{e}_{\varphi} = -\sin\varphi\,\boldsymbol{e}_x + \cos\varphi\,\boldsymbol{e}_y, \tag{2.33}$$
$$\boldsymbol{e}_z = \boldsymbol{e}_z, \tag{2.34}$$
$$\boldsymbol{e}_r = \sin\theta\cos\varphi\,\boldsymbol{e}_x + \sin\theta\sin\varphi\,\boldsymbol{e}_y + \cos\theta\,\boldsymbol{e}_z, \tag{2.35}$$
$$\boldsymbol{e}_{\theta} = \cos\theta\cos\varphi\,\boldsymbol{e}_x + \cos\theta\sin\varphi\,\boldsymbol{e}_y - \sin\theta\,\boldsymbol{e}_z. \tag{2.36}$$

Hence, the zeroth-order velocity field admits the following asymptotic representation:

$$\boldsymbol{u}^{(0,0)} = \left(\frac{\alpha\dot{m}^{\star}}{4\pi\,\mathscr{D}\mu U^{\star}\ell}\right)\left\{\frac{1}{r}\left[(1+2\cos\theta)\,\boldsymbol{e}_r + \frac{\sin\theta\cos\theta}{1-\cos\theta}\boldsymbol{e}_{\theta}\right]\right\} + \mathscr{O}(r^{-2}), \tag{2.37}$$

which agrees with the expression reported by Würger (2014).

Next, we seek the solution of (2.24) for $\tilde{\boldsymbol{u}}^{(0,1)}$. As will become clear shortly, it is advantageous to again work in the Fourier space. Hence, following Masoud & Shelley

https://doi.org/10.1017/jfm.2025.11027 Published online by Cambridge University Press

(2014), we rewrite the governing equations as

$$\left(\frac{\partial^2}{\partial\tilde{z}^2}-\tilde{k}^2+\boldsymbol{e}_x\cdot i\tilde{\boldsymbol{k}}\right)\left(\widehat{\tilde{u}}_x^{(0,1)}\boldsymbol{e}_x+\widehat{\tilde{u}}_y^{(0,1)}\boldsymbol{e}_y\right)=i\tilde{\boldsymbol{k}}\widehat{\tilde{p}}^{(0,1)}, \tag{2.38}$$

$$\left(\frac{\partial^2}{\partial\tilde{z}^2}-\tilde{k}^2+\boldsymbol{e}_x\cdot i\tilde{\boldsymbol{k}}\right)\widehat{\tilde{u}}_z^{(0,1)}=\frac{\partial\widehat{\tilde{p}}^{(0,1)}}{\partial\tilde{z}}, \tag{2.39}$$

$$i\tilde{\boldsymbol{k}}\cdot\left(\widehat{\tilde{u}}_x^{(0,1)}\boldsymbol{e}_x+\widehat{\tilde{u}}_y^{(0,1)}\boldsymbol{e}_y\right)+\frac{\partial\widehat{\tilde{u}}_z^{(0,1)}}{\partial\tilde{z}}=0, \tag{2.40}$$

$$\left(\frac{\partial^2}{\partial\tilde{z}^2}-\tilde{k}^2\right)\widehat{\tilde{p}}^{(0,1)}=0, \tag{2.41}$$

subject to the boundary conditions

$$\widehat{\tilde{u}}_z^{(0,1)}\Big|_{\tilde{z}=0}=0, \tag{2.42}$$

$$\frac{\partial\widehat{\tilde{u}}_x^{(0,1)}}{\partial\tilde{z}}\Big|_{\tilde{z}=0}\boldsymbol{e}_x+\frac{\partial\widehat{\tilde{u}}_y^{(0,1)}}{\partial\tilde{z}}\Big|_{\tilde{z}=0}\boldsymbol{e}_y=-\left(\frac{\alpha\dot{m}^\star}{\mathscr{D}\mu U^\star\ell}\right)\frac{i\tilde{\boldsymbol{k}}}{\tilde{k}}. \tag{2.43}$$

The solutions to this coupled system can be expressed in terms of the interfacial velocity, $\widehat{\tilde{\boldsymbol{u}}}_s^{(0,1)}=\widehat{\tilde{u}}_x^{(0,1)}\big|_{\tilde{z}=0}\boldsymbol{e}_x+\widehat{\tilde{u}}\big|_{\tilde{z}=0}\boldsymbol{e}_y$:

$$\widehat{\tilde{p}}^{(0,1)}=\frac{\boldsymbol{e}_x\cdot i\tilde{\boldsymbol{k}}}{\tilde{k}}\frac{i\tilde{\boldsymbol{k}}\cdot\widehat{\tilde{\boldsymbol{u}}}_s^{(0,1)}}{\sqrt{\tilde{k}^2-\boldsymbol{e}_x\cdot i\tilde{\boldsymbol{k}}}-\tilde{k}}\exp(\tilde{k}\tilde{z}), \tag{2.44}$$

$$\widehat{\tilde{u}}_z^{(0,1)}=\frac{i\tilde{\boldsymbol{k}}\cdot\widehat{\tilde{\boldsymbol{u}}}_s^{(0,1)}}{\sqrt{\tilde{k}^2-\boldsymbol{e}_x\cdot i\tilde{\boldsymbol{k}}}-\tilde{k}}\left[\exp(\tilde{k}z)-\exp\left(\sqrt{\tilde{k}^2-\boldsymbol{e}_x\cdot i\tilde{\boldsymbol{k}}}\,\tilde{z}\right)\right], \tag{2.45}$$

$$\widehat{\tilde{u}}_x^{(0,1)}\boldsymbol{e}_x+\widehat{\tilde{u}}_y^{(0,1)}\boldsymbol{e}_y=\frac{i\tilde{\boldsymbol{k}}}{\tilde{k}}\widehat{\tilde{u}}_z^{(0,1)}+\widehat{\tilde{\boldsymbol{u}}}_s^{(0,1)}\exp\left(\sqrt{\tilde{k}^2-\boldsymbol{e}_x\cdot i\tilde{\boldsymbol{k}}}\,\tilde{z}\right). \tag{2.46}$$

Taking the derivative of the in-plane velocity and evaluating it at $\tilde{z}=0$, we obtain

$$\begin{aligned}\frac{\partial\widehat{\tilde{u}}_x^{(0,1)}}{\partial\tilde{z}}\Big|_{\tilde{z}=0}\boldsymbol{e}_x+\frac{\partial\widehat{\tilde{u}}_y^{(0,1)}}{\partial\tilde{z}}\Big|_{\tilde{z}=0}\boldsymbol{e}_y&=\sqrt{\tilde{k}^2-\boldsymbol{e}_x\cdot i\tilde{\boldsymbol{k}}}\left(\boldsymbol{I}+\frac{\tilde{\boldsymbol{k}}\tilde{\boldsymbol{k}}}{\tilde{k}\sqrt{\tilde{k}^2-\boldsymbol{e}_x\cdot i\tilde{\boldsymbol{k}}}}\right)\cdot\widehat{\tilde{\boldsymbol{u}}}_s^{(0,1)}\\&=-\left(\frac{\alpha\dot{m}^\star}{\mathscr{D}\mu U^\star\ell}\right)\frac{i\tilde{\boldsymbol{k}}}{\tilde{k}}.\end{aligned} \tag{2.47}$$

Solving for $\widehat{\tilde{\boldsymbol{u}}}_s^{(0,1)}$, we find

$$\begin{aligned}\widehat{\tilde{\boldsymbol{u}}}_s^{(0,1)}&=\left\{\frac{1}{\sqrt{\tilde{k}^2-\boldsymbol{e}_x\cdot i\tilde{\boldsymbol{k}}}}\left[\boldsymbol{I}-\frac{\tilde{\boldsymbol{k}}\tilde{\boldsymbol{k}}}{\tilde{k}\left(\sqrt{\tilde{k}^2-\boldsymbol{e}_x\cdot i\tilde{\boldsymbol{k}}}+\tilde{k}\right)}\right]\right\}\cdot\left[-\left(\frac{\alpha\dot{m}^\star}{\mathscr{D}\mu U^\star\ell}\right)\frac{i\tilde{\boldsymbol{k}}}{k}\right]\\&=-\left(\frac{\alpha\dot{m}^\star}{\mathscr{D}\mu U^\star\ell}\right)\frac{1}{\sqrt{\tilde{k}^2-\boldsymbol{e}_x\cdot i\tilde{\boldsymbol{k}}}+\tilde{k}}\frac{i\tilde{\boldsymbol{k}}}{\tilde{k}}.\end{aligned} \tag{2.48}$$

https://doi.org/10.1017/jfm.2025.11027 Published online by Cambridge University Press

Finally, substituting back into (2.45) and (2.46), the full velocity field is given by

$$\widehat{\tilde{\boldsymbol{u}}}^{(0,1)} = -\left(\frac{\alpha\dot{m}^\star}{\mathscr{D}\mu U^\star\ell}\right)\frac{1}{\boldsymbol{e}_x\cdot i\tilde{\boldsymbol{k}}}\left\{i\tilde{\boldsymbol{k}}\left[\exp(\tilde{k}\tilde{z}) - \sqrt{1-\boldsymbol{e}_x\cdot i\tilde{\boldsymbol{k}}/\tilde{k}^2}\,\exp\left(\sqrt{\tilde{k}^2-\boldsymbol{e}_x\cdot i\tilde{\boldsymbol{k}}}\,\tilde{z}\right)\right]\right.$$
$$\left. + \tilde{k}\left[\exp(\tilde{k}\tilde{z}) - \exp\left(\sqrt{\tilde{k}^2-\boldsymbol{e}_x\cdot i\tilde{\boldsymbol{k}}}\,\tilde{z}\right)\right]\boldsymbol{e}_z\right\}. \tag{2.49}$$

The conversion to real space for this velocity correction is not needed, as the subsequent integrals involving this velocity in the evaluation of the propulsion speed are performed in Fourier space.

2.4. *Behaviour of the propulsion speed in the limits of low Péclet and Reynolds numbers*

By substituting the auxiliary velocity field $\boldsymbol{u}_a$, along with the asymptotic expansions for the concentration and velocity fields, into (2.10*c*), we obtain an asymptotic expression for the normalised propulsion speed of the surfer

$$\begin{aligned}\mathscr{U} &= \mathscr{U}^{(0,0)} + Pe\ln Pe\,\mathscr{U}^{(1,0)} + Re\ln Re\,\mathscr{U}^{(0,1)} + \mathscr{O}(Pe) + \mathscr{O}(Re)\\ &= 1 - \frac{\alpha\dot{m}^\star}{32\pi\mathscr{D}\mu U^\star\ell}\,(2\,Pe\ln Pe + Re\ln Re) + \mathscr{O}(Pe) + \mathscr{O}(Re).\end{aligned} \tag{2.50}$$

In what follows, we outline the derivation of the leading-order correction terms that appear in (2.50).

2.4.1. *Derivation of the leading-order Pe correction*

To isolate the leading-order correction due to *Pe*, we begin by setting $Re = 0$, which reduces (2.10*c*) to

$$\mathscr{U} = -\int_{S_i}(\gamma-\gamma_0)\,\nabla_{S_i}\cdot\left(\frac{\boldsymbol{u}_a}{F_a}\right)\mathrm{d}S. \tag{2.51}$$

Next, we replace for $\gamma-\gamma_0$ from (2.13), (2.14), and (2.19)–(2.21) to arrive at

$$\mathscr{U} = 1 + \frac{\alpha\dot{m}^\star Pe}{2\pi\mathscr{D}\mu U^\star\ell}\left[\int_{S_i} c^{(1,0)}\,\nabla_{S_i}\cdot\left(\frac{\boldsymbol{u}_a}{F_a}\right)\mathrm{d}S\right.$$
$$\left. + \int_{S_i}\left(\check{c}^{(1,0)} - \check{c}^{(0,0)}_\infty - \check{c}^{(1,0)}_\infty\right)\check{\nabla}_{S_i}\cdot\left(\frac{{}^{-1}\check{\boldsymbol{u}}_a}{F_a}\right)\mathrm{d}\check{S}\right] + \cdots, \tag{2.52}$$

where the ellipsis denotes terms of higher order in *Pe* beyond those explicitly retained, and the base speed $U^\star$ is determined by

$$U^\star = \frac{\alpha\dot{m}^\star}{2\pi\mathscr{D}\mu\ell}\int_{S_i} c^{(0,0)}\,\nabla_{S_i}\cdot\left(\frac{\boldsymbol{u}_a}{F_a}\right)\mathrm{d}S. \tag{2.53}$$

Additionally, we use the relation

$$\left[\nabla_{S_i}\cdot\left(\frac{{}^{-1}\boldsymbol{u}_a}{F_a}\right)\right]_{z=0} = -\frac{x}{4\pi\rho^3} = -\frac{\cos\varphi}{4\pi\rho^2}. \tag{2.54}$$

The integral involving $c^{(1,0)}$ can be split into two parts: one over the region between the closed contour l_p and a circle of radius 1 (denoted by $S_i^{(\rho<1)}$), and the other over the

https://doi.org/10.1017/jfm.2025.11027 Published online by Cambridge University Press

annular region extending from radius 1 to ∞. Making this division and noting that

$$\left[c^{(1,0)}\,\boldsymbol{\nabla}_{S_i}\cdot\left(\frac{\boldsymbol{u}_a}{F_a}\right)\right]_{z=0}=\frac{\cos\varphi}{8\pi\rho^2}\,(1+\cos\varphi)+\mathscr{O}(\rho^{-3}),\tag{2.55}$$

we reach

$$\begin{aligned}\int_{S_i} c^{(1,0)}\,\boldsymbol{\nabla}_{S_i}\cdot\left(\frac{\boldsymbol{u}_a}{F_a}\right)\mathrm{d}S&=\int_{S_i^{(\rho<1)}} c^{(1,0)}\,\boldsymbol{\nabla}_{S_i}\cdot\left(\frac{\boldsymbol{u}_a}{F_a}\right)\mathrm{d}S\\&\quad+\int_1^\infty\int_0^{2\pi}\left[c^{(1,0)}\,\boldsymbol{\nabla}_{S_i}\cdot\left(\frac{\boldsymbol{u}_a}{F_a}\right)\right]_{z=0}\rho\,\mathrm{d}\varphi\,\mathrm{d}\rho\\&=\frac{1}{8}\int_1^\infty\frac{1}{\rho}\,\mathrm{d}\rho+\mathscr{O}(1).\end{aligned}\tag{2.56}$$

The near-field integral is $\mathscr{O}(1)$ because all quantities appearing in the integrand remain finite in the near-field region, and the integration domain itself is bounded. Similarly, the second integral on the right-hand side of (2.52) can be simplified to

$$\begin{aligned}&\int_{S_i}\left(\check{c}^{(1,0)}-\check{c}^{(0,0)}_\infty-\check{c}^{(1,0)}_\infty\right)\check{\boldsymbol{\nabla}}_{S_i}\cdot\left(\frac{-1\check{\boldsymbol{u}}_a}{F_a}\right)\mathrm{d}\check{S}\\&=\int_{S_i^{(\rho<1)}}\left(\check{c}^{(1,0)}-\check{c}^{(0,0)}_\infty-\check{c}^{(1,0)}_\infty\right)\check{\boldsymbol{\nabla}}_{S_i}\cdot\left(\frac{-1\check{\boldsymbol{u}}_a}{F_a}\right)\mathrm{d}\check{S}\\&\quad-\frac{1}{4\pi}\int_{Pe}^\infty\int_0^{2\pi}\left(\check{c}^{(1,0)}-\check{c}^{(0,0)}_\infty-\check{c}^{(1,0)}_\infty\right)\frac{\cos\varphi}{\check{\rho}}\,\mathrm{d}\varphi\,\mathrm{d}\check{\rho}\\&=-\frac{1}{4\pi}\int_0^\infty\int_0^{2\pi}\left(\check{c}^{(1,0)}-\check{c}^{(0,0)}_\infty-\check{c}^{(1,0)}_\infty\right)\frac{\cos\varphi}{\check{\rho}}\,\mathrm{d}\varphi\,\mathrm{d}\check{\rho}+\mathscr{O}(Pe)\\&=-\frac{1}{8}\int_1^\infty\frac{1}{\check{\rho}}\,\mathrm{d}\check{\rho}+\mathscr{O}(1)=-\frac{1}{8}\int_{1/Pe}^\infty\frac{1}{\rho}\,\mathrm{d}\rho+\mathscr{O}(1).\end{aligned}\tag{2.57}$$

Note that, when transitioning from the third to the fourth line, the lower limit of integration with respect to $\check{\rho}$ is extended from Pe to 0. The resulting contribution from the added interval $0\leqslant\check{\rho}<Pe$ (which also includes the integral in the second line) is $\mathscr{O}(Pe)$, since $\left(\check{c}^{(1,0)}-\check{c}^{(0,0)}_\infty-\check{c}^{(1,0)}_\infty\right)\sim\mathscr{O}(\check{\rho})$ as $\check{\rho}\to 0$. Substituting (2.56) and (2.57) into (2.52), it follows that

$$\mathscr{U}^{(1,0)}=-\frac{\alpha\dot{m}^\star}{16\pi\mathscr{D}\mu U^\star\ell}.\tag{2.58}$$

2.4.2. *Derivation of the leading-order Re correction*

Once again, we invoke the integral identity in (2.10*c*), this time setting $Pe=0$, which simplifies the expression to

$$\mathscr{U}=1+Re\left[\int_V\boldsymbol{u}\cdot\boldsymbol{\nabla}\left(\frac{\boldsymbol{u}_a}{F_a}\right)\cdot\boldsymbol{u}\,\mathrm{d}V-\mathscr{U}\boldsymbol{e}_x\cdot\int_V\boldsymbol{\nabla}\left(\frac{\boldsymbol{u}_a}{F_a}\right)\cdot\boldsymbol{u}\,\mathrm{d}V\right].\tag{2.59}$$

https://doi.org/10.1017/jfm.2025.11027 Published online by Cambridge University Press

To evaluate the above integrals, we insert the velocity expansion from (2.15). Considering the far-field behaviour of $\boldsymbol{u}^{(0,0)}$ from (2.37), for the first integral, we find

$$\int_V \boldsymbol{u}\cdot\boldsymbol{\nabla}\Big(\frac{\boldsymbol{u}_a}{F_a}\Big)\cdot\boldsymbol{u}\,\mathrm{d}V = \underbrace{\int_V \boldsymbol{u}^{(0,0)}\cdot\boldsymbol{\nabla}\Big(\frac{\boldsymbol{u}_a}{F_a}\Big)\cdot\boldsymbol{u}^{(0,0)}\,\mathrm{d}V}_{\mathscr{O}(1)} + \mathscr{O}(Re\ln Re). \tag{2.60}$$

Proceeding to the second integral, we obtain

$$\begin{aligned}\mathscr{U}\boldsymbol{e}_x\cdot\int_V \boldsymbol{\nabla}\Big(\frac{\boldsymbol{u}_a}{F_a}\Big)\cdot\boldsymbol{u}\,\mathrm{d}V &= \underbrace{\int_V \boldsymbol{e}_x\cdot\left[\boldsymbol{\nabla}\Big(\frac{\boldsymbol{u}_a}{F_a}\Big)\cdot\boldsymbol{u}^{(0,0)} - \boldsymbol{\nabla}\Big(\frac{{}_{-1}\boldsymbol{u}_a}{F_a}\Big)\cdot\boldsymbol{u}_\infty^{(0,0)}\right]\mathrm{d}V}_{\mathscr{O}(1)}\\ &\quad + \int_V \boldsymbol{e}_x\cdot\tilde{\boldsymbol{\nabla}}\Big(\frac{{}_{-1}\tilde{\boldsymbol{u}}_a}{F_a}\Big)\cdot\tilde{\boldsymbol{u}}^{(0,1)}\,\mathrm{d}\tilde{V} + \mathscr{O}(Re\ln Re),\end{aligned} \tag{2.61}$$

where $\boldsymbol{u}_\infty^{(0,0)} = {}_{-1}\boldsymbol{u}^{(0,0)}$. The second integral on the right-hand side of (2.61) can be recast as

$$\begin{aligned}\int_V \boldsymbol{e}_x\cdot\tilde{\boldsymbol{\nabla}}\Big(\frac{{}_{-1}\tilde{\boldsymbol{u}}_a}{F_a}\Big)\cdot\tilde{\boldsymbol{u}}^{(0,1)}\,\mathrm{d}\tilde{V} &= -\int_{\mathscr{V}^{(r<1)}} \boldsymbol{e}_x\cdot\tilde{\boldsymbol{\nabla}}\Big(\frac{{}_{-1}\tilde{\boldsymbol{u}}_a}{F_a}\Big)\cdot\tilde{\boldsymbol{u}}^{(0,1)}\,\mathrm{d}\tilde{V}\\ &\quad + \int_{\mathscr{V}} \boldsymbol{e}_x\cdot\tilde{\boldsymbol{\nabla}}\Big(\frac{{}_{-1}\tilde{\boldsymbol{u}}_a}{F_a}\Big)\cdot\tilde{\boldsymbol{u}}^{(0,1)}\,\mathrm{d}\tilde{V}\\ &\quad + \underbrace{\int_{V^{(r<1)}} \boldsymbol{e}_x\cdot\tilde{\boldsymbol{\nabla}}\Big(\frac{{}_{-1}\tilde{\boldsymbol{u}}_a}{F_a}\Big)\cdot\tilde{\boldsymbol{u}}^{(0,1)}\,\mathrm{d}\tilde{V}}_{\mathscr{O}(1)},\end{aligned} \tag{2.62}$$

with

$$\begin{aligned}\mathscr{V} &= \{\boldsymbol{r}\in\mathbb{R}^3 : z\leqslant 0\},\\ \mathscr{V}^{(r<1)} &= \{\boldsymbol{r}\in\mathbb{R}^3 : z\leqslant 0,\ r<1\},\\ V^{(r<1)} &= \{\boldsymbol{r}\in V : r<1\}.\end{aligned} \tag{2.63}$$

Recalling the matching condition (2.27), the first term on the right-hand side of (2.62) becomes

$$\int_{\mathscr{V}^{(r<1)}} \boldsymbol{e}_x\cdot\tilde{\boldsymbol{\nabla}}\Big(\frac{{}_{-1}\tilde{\boldsymbol{u}}_a}{F_a}\Big)\cdot\tilde{\boldsymbol{u}}^{(0,1)}\,\mathrm{d}\tilde{V} = \int_{\mathscr{V}^{(r<1)}} \boldsymbol{e}_x\cdot\boldsymbol{\nabla}\Big(\frac{{}_{-1}\boldsymbol{u}_a}{F_a}\Big)\cdot\boldsymbol{u}_\infty^{(0,0)}\,\mathrm{d}V + \mathscr{O}(Re\ln Re), \tag{2.64}$$

where, given that

$$\boldsymbol{e}_x\cdot\boldsymbol{\nabla}\Big(\frac{{}_{-1}\boldsymbol{u}_a}{F_a}\Big) = \frac{1-3\sin^2\theta\cos^2\varphi}{4\pi r^2}\,\boldsymbol{e}_r, \tag{2.65}$$

the right-hand-side integral equals to

$$\begin{aligned}&\Big(\frac{\alpha\dot{m}^\star}{16\pi^2\mathscr{D}\mu U^\star\ell}\Big)\int_0^1\int_0^{2\pi}\int_{\pi/2}^{\pi}\Big(1-3\sin^2\theta\cos^2\varphi\Big)\frac{\sin\theta+\sin 2\theta}{r}\,\mathrm{d}\theta\,\mathrm{d}\varphi\,\mathrm{d}r\\ &= -\Big(\frac{\alpha\dot{m}^\star}{32\pi\mathscr{D}\mu U^\star\ell}\Big)\int_0^1\frac{1}{r}\,\mathrm{d}r = -\Big(\frac{\alpha\dot{m}^\star}{32\pi\mathscr{D}\mu U^\star\ell}\Big)\int_1^\infty\frac{1}{r}\,\mathrm{d}r.\end{aligned} \tag{2.66}$$

https://doi.org/10.1017/jfm.2025.11027 Published online by Cambridge University Press

To calculate the second integral in (2.62), we use the two-dimensional Fourier convolution theorem (see, e.g. Masoud & Stone 2019, p. 39) as follows:

$$\int_{\mathscr{V}} \boldsymbol{e}_x \cdot \tilde{\boldsymbol{\nabla}}\left(\frac{{}_{-1}\tilde{\boldsymbol{u}}_a}{F_a}\right) \cdot \tilde{\boldsymbol{u}}^{(0,1)}\, \mathrm{d}\tilde{V} = \int_{-\infty}^{0}\int_{\mathbb{R}^2} \boldsymbol{e}_x \cdot \tilde{\boldsymbol{\nabla}}\left(\frac{{}_{-1}\tilde{\boldsymbol{u}}_a}{F_a}\right) \cdot \tilde{\boldsymbol{u}}^{(0,1)}\, \mathrm{d}\tilde{\boldsymbol{\rho}}\, \mathrm{d}\tilde{z}$$

$$= \frac{1}{(2\pi)^2}\int_{-\infty}^{0}\int_{\mathbb{R}^2} \left(\boldsymbol{e}_x \cdot i\tilde{\boldsymbol{k}}\right)\mathfrak{F}_{xy}\left\{\frac{{}_{-1}\tilde{\boldsymbol{u}}_a}{F_a}\right\}(\tilde{\boldsymbol{k}}) \cdot \mathfrak{F}_{xy}\{\tilde{\boldsymbol{u}}^{(0,1)}\}(-\tilde{\boldsymbol{k}})\, \mathrm{d}\tilde{\boldsymbol{k}}\, \mathrm{d}\tilde{z}, \tag{2.67}$$

where $\tilde{\boldsymbol{k}} = \boldsymbol{k}/Re$ and the Fourier transform of the auxiliary velocity field is given by

$$\mathfrak{F}_{xy}\left\{\frac{{}_{-1}\tilde{\boldsymbol{u}}_a}{F_a}\right\} = \exp(\tilde{k}\tilde{z})\left\{\left[\boldsymbol{I} + \frac{\tilde{\boldsymbol{k}}\tilde{\boldsymbol{k}}}{2\tilde{k}^2}\left(\tilde{k}\tilde{z}-1\right)\right]\cdot\frac{\boldsymbol{e}_x}{\tilde{k}} - \frac{i\tilde{\boldsymbol{k}}\cdot\boldsymbol{e}_x}{2\tilde{k}}\tilde{z}\,\boldsymbol{e}_z,\right\}. \tag{2.68}$$

This expression can be derived by rewriting the $\mathscr{O}(r^{-1})$ component of the auxiliary velocity field via Bessel integral representations (see Gradshteyn & Ryzhik 2007; Baddour 2011, 6.611-1,6.621-4,6.623-3)

$$\frac{{}_{-1}\boldsymbol{u}_a}{F_a} = \frac{1}{2\pi}\left[\int_0^\infty \exp(kz)\,J_0(k\rho)\,\mathrm{d}k\,\boldsymbol{e}_x - \boldsymbol{\nabla}_{xy}\boldsymbol{\nabla}_{xy}\cdot\boldsymbol{e}_x\int_0^\infty \frac{\exp(kz)\,(kz-1)}{2k^2}J_0(k\rho)\,\mathrm{d}k\right.$$
$$\left. - \frac{z}{2}\,\boldsymbol{\nabla}_{xy}\cdot\boldsymbol{e}_x\int_0^\infty \exp(kz)\,J_0(k\rho)\,\mathrm{d}k\,\boldsymbol{e}_z\right]. \tag{2.69}$$

Alternatively, (2.68) may be obtained by employing the approach of Masoud & Shelley (2014) (see also § 2.3.2). Replacing for $\mathfrak{F}_{xy}\{{}_{-1}\tilde{\boldsymbol{u}}_a/F_a\}$ in (2.67) from (2.68) and simplifying yields

$$\left(\frac{\mathscr{D}\mu U^\star \ell}{\alpha \dot{m}^\star}\right)\int_{-\infty}^{0}\int_{\mathbb{R}^2}\left(\boldsymbol{e}_x\cdot i\tilde{\boldsymbol{k}}\right)\mathfrak{F}_{xy}\left\{\frac{{}_{-1}\tilde{\boldsymbol{u}}_a}{F_a}\right\}(\tilde{\boldsymbol{k}})\cdot\mathfrak{F}_{xy}\{\tilde{\boldsymbol{u}}^{(1)}\}(-\tilde{\boldsymbol{k}})\,\mathrm{d}\tilde{\boldsymbol{k}}\,\mathrm{d}\tilde{z}$$
$$= -\frac{1}{2}\int_{-\infty}^{0}\int_{\mathbb{R}^2}\left(\boldsymbol{e}_x\cdot i\tilde{\boldsymbol{k}}\right)\exp(\tilde{k}\tilde{z})$$
$$\times\left\{\left(2\tilde{z}+\frac{1}{\tilde{k}}\right)\exp(\tilde{k}\tilde{z}) - \left[\left(\tilde{z}+\frac{1}{\tilde{k}}\right)\frac{\sqrt{\tilde{k}^2+\boldsymbol{e}_x\cdot i\tilde{\boldsymbol{k}}}}{\tilde{k}}+\tilde{z}\right]\exp\left(\sqrt{\tilde{k}^2+\boldsymbol{e}_x\cdot i\tilde{\boldsymbol{k}}}\,\tilde{z}\right)\right\}\mathrm{d}\tilde{\boldsymbol{k}}\,\mathrm{d}\tilde{z}. \tag{2.70a}$$

Carrying out the z-integration and simplifying further gives

$$\int_{\mathbb{R}^2} 1-\sqrt{1+\frac{\boldsymbol{e}_x\cdot i\tilde{\boldsymbol{k}}}{\tilde{k}^2}}+\frac{\boldsymbol{e}_x\cdot i\tilde{\boldsymbol{k}}}{2\tilde{k}^2}\,\mathrm{d}\tilde{\boldsymbol{k}} = \int_0^\infty\int_0^{2\pi}\left(1-\sqrt{1+\frac{i\cos\phi}{\tilde{k}}}+\frac{i\cos\phi}{2\tilde{k}}\right)\tilde{k}\,\mathrm{d}\phi\,\mathrm{d}\tilde{k}, \tag{2.70b}$$

where $\phi = \tan^{-1}(k_y/k_x)$ is the polar angle in the two-dimensional Fourier space. We decompose the integral on the right-hand side into two regions

$$\underbrace{\int_0^1\int_0^{2\pi}\left(1-\sqrt{1+\frac{i\cos\phi}{\tilde{k}}}\right)\tilde{k}\,\mathrm{d}\phi\,\mathrm{d}\tilde{k}}_{\mathscr{O}(1)} + \int_1^\infty\int_0^{2\pi}\left(1-\sqrt{1+\frac{i\cos\phi}{\tilde{k}}}\right)\tilde{k}\,\mathrm{d}\phi\,\mathrm{d}\tilde{k}. \tag{2.70c}$$

https://doi.org/10.1017/jfm.2025.11027 Published online by Cambridge University Press

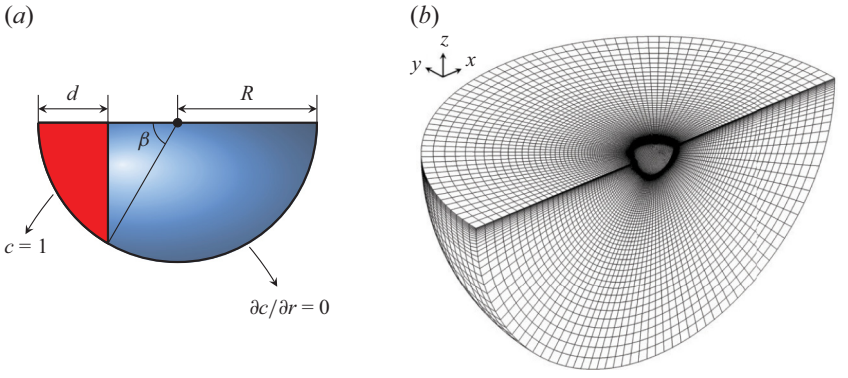


Figure 2. (*a*) Concentration boundary condition on the wet surface of the model spherical surfer in the numerical simulations, where the active area of S_p is coloured red. (*b*) A representative portion of the computational domain. For clarity, the full domain is not shown.

Expanding the square root in the second integral as

$$\sqrt{1+x} = 1 + \frac{1}{2}x - \frac{1}{8}x^2 + \frac{1}{16}x^3 - \frac{5}{128}x^4 + \cdots, \tag{2.70d}$$

and retaining the leading contribution, we then obtain

$$\begin{aligned}\int_1^\infty \int_0^{2\pi} \left(1 - \sqrt{1 + \frac{i\cos\phi}{\tilde{k}}}\right) \tilde{k}\, \mathrm{d}\phi\, \mathrm{d}\tilde{k} &= -\frac{\pi}{8}\int_1^\infty \frac{1}{\tilde{k}}\, \mathrm{d}\tilde{k} + \mathscr{O}(1) \\ &= -\frac{\pi}{8}\int_{Re}^\infty \frac{1}{k}\, \mathrm{d}k + \mathscr{O}(1).\end{aligned} \tag{2.70e}$$

Combining the results of (2.66) and (2.70*e*), we find that

$$\mathscr{U}^{(0,1)} = -\frac{\alpha \dot{m}^\star}{32\pi \mathscr{D}\mu U^\star \ell}. \tag{2.71}$$

3. Numerical solution

To assess the validity range of our theoretical predictions and to examine the propulsion behaviour of the Marangoni surfer across a broad spectrum of Péclet and Reynolds numbers, we numerically compute the propulsion speed of a representative half-submerged spherical surfer. The model surfer consists of an active region maintained at a fixed concentration and an inactive region subject to a no-flux boundary condition (see figure 2*a* and also Masoud & Rothstein 2022). We adopt the second-order finite-volume method developed by Jafari Kang *et al.* (2020), in which the coupled advection–diffusion and Navier–Stokes equations are solved until the steady state is reached in a non-inertial reference frame moving with the particle.

Implemented in OpenFOAM, this approach discretises the spatial derivatives (gradients and Laplacians) using the second-order linear Gaussian integration scheme. Surface-normal gradients are evaluated using a corrected scheme with one or two corrections depending on mesh non-orthogonality. Temporal derivatives are approximated via the second-order backward differentiation formula. The particle's translational motion is integrated using the Newmark method with a relaxation parameter of 1/2. Pressure–velocity coupling is handled using the PIMPLE algorithm (a combination of PISO (Pressure Implicit with Splitting of Operator) and SIMPLE (Semi-Implicit Method for Pressure-Linked Equations) algorithms), while the pressure field is solved using

https://doi.org/10.1017/jfm.2025.11027 Published online by Cambridge University Press

the GAMG (geometric-algebraic multigrid) solver with a DIC (diagonal incomplete-Cholesky) preconditioner. The velocity and concentration fields are obtained through Gauss–Seidel iterations.

The computational domain is constructed as a large hemisphere with the submerged portion of the surfer removed from its top centre (see figure 2*b*; for clarity, only a portion of the full domain is shown). This set-up enables the use of a sweeping meshing technique, which produces a high-quality grid with enhanced resolution near the interface and the surfer, where steep gradients are expected. The default domain radius is a hundred times the radius of the surfer, but it is increased tenfold when either the Péclet or Reynolds number is sufficiently small (i.e. $Pe \lesssim 10^{-2}$ or $Re \lesssim 10^{-2}$) to minimise the influence of the outer boundary and approximate an unconfined environment. Inlet and outlet boundary conditions are applied to the front and back faces of the domain. Grid independence is verified through systematic mesh refinement, and in all cases, the chosen mesh ensures that further refinement produces negligible changes in the computed propulsion speed. The outlined numerical framework has been previously validated against both analytical predictions and experimental measurements (Jafari Kang *et al.* 2020), demonstrating its reliability across the parameter regimes of interest.

4. Results and discussion

We begin by examining the structure and implications of the asymptotic formula for the normalised propulsion speed. Specifically, we have shown that when both Pe and Re are small, the normalised speed admits the form

$$\mathscr{U} = 1 + \mathscr{A}(2\,Pe \ln Pe + Re \ln Re) + \cdots. \tag{4.1}$$

It is worth emphasising that expression (4.1) is fully generic: the logarithmic dependence on Pe and Re originates from the far-field asymptotics of the governing advection–diffusion and momentum equations and therefore holds for surfers of arbitrary shape. The specific particle geometry and discharge pattern enter the result only through the multiplier $\mathscr{A}$, which encapsulates all shape- and mechanism-dependent information.

The sign of $\mathscr{A}$ is opposite to that of α (see also (2.50)), the negative of the slope of the surface-tension–concentration relation (see (2.13)). That is, if the release of the chemical agent locally reduces surface tension ($\alpha > 0$), then $\mathscr{A} < 0$ and the normalised speed $\mathscr{U}$ exceeds unity (noting that $\ln x < 0$ for $x < 1$). Conversely, when $\alpha < 0$ (i.e. the agent increases surface tension), the propulsion speed falls below its baseline value. This dichotomy has a clear physical interpretation: when the active region of the surfer reduces local surface tension, the resulting Marangoni stress pushes the fluid outward from the active zone. On the other hand, if the active region increases surface tension, the surrounding fluid is pulled inward. These flow signatures are qualitatively reminiscent of extensile (pusher-like) and contractile (puller-like) patterns observed in bulk microswimmers.

This analogy with bulk microswimmers extends further. For example, in the limit of weak inertia, the propulsion speed of squirmers varies linearly with Re, increasing for pushers and decreasing for pullers (see, e.g. Chisholm *et al.* 2016). Similarly, for autophoretic Janus particles, the speed depends linearly on Pe when advection remains subdominant, with the sign of the correction governed by the particle's mobility coefficient (see, e.g. Michelin & Lauga 2014). In our case, however, the leading-order corrections scale as $Pe \ln Pe$ and $Re \ln Re$, indicating a stronger sensitivity to advective effects than in bulk self-propulsion. This logarithmic enhancement amplifies the influence of even small Pe and Re, making convective and inertial corrections more significant than one might expect. The asymptotic expression thus encapsulates not only the

https://doi.org/10.1017/jfm.2025.11027 Published online by Cambridge University Press

	$\frac{d}{R}$	$Pe = 10^{-2}$ $Re = 10^{-2}$	$Pe = 10^{-1}$ $Re = 10^{-2}$	$Pe = 10^{-2}$ $Re = 10^{-1}$	$Pe = 10^{-1}$ $Re = 10^{-1}$
Theory	1/2	1.13	1.49	1.31	1.67
Simulation	1/2	1.10	1.43	1.29	1.61
Difference (%)		2.68	4.03	1.55	3.98
Theory	1	1.23	1.86	1.55	2.17
Simulation	1	1.19	1.83	1.58	2.16
Difference (%)		3.28	1.55	2.28	0.29
Theory	3/2	1.54	2.99	2.26	3.71
Simulation	3/2	1.49	2.89	2.59	3.86
Difference (%)		3.66	3.14	12.76	3.89

Table 1. Comparison between the numerically calculated and theoretically obtained results for the normalised propulsion speed ($\mathscr{U}$) of the model surfer for three release configurations corresponding to $d/R = 1/2$, 1, and 3/2 (see figure 2*a*). The dimensionless propulsion speed ($\mathbb{U}^\star = \mu\, U^\star/\alpha\, \underset{\sim}{c}_s$), Sherwood number ($Sh^\star$) and multiplier $\mathscr{A}$ for these cases are reported in table 2.

direction of the effect (enhancement or retardation) but also the non-trivial dependence on physicochemical parameters, offering actionable insight for optimising surfer design through geometry, size, surfactant properties and agent release strategy.

To assess the accuracy of these theoretical predictions, we compare them against numerical simulations. These tests are conducted for a half-submerged spherical surfer of radius R (note that $\ell = R$ for a sphere), featuring active surface regions of widths $d/R = 1 - \cos\beta = 1/2$, 1 and 3/2 (see figure 2*a* for the graphical definition of β), across four combinations of $Pe = 10^{-2}$ or 10^{-1} and $Re = 10^{-2}$ or 10^{-1}. While our asymptotic theory applies generally to both signs of α, we restrict our comparison to the more practical case of $\alpha > 0$ for brevity. As summarised in table 1, the predicted and simulated values of $\mathscr{U}$ agree closely, with relative discrepancies typically below 5 %. This close match not only validates the numerical framework but also supports the fidelity of the perturbative theoretical analysis. Although omitted here to avoid redundancy, we have also verified that the theoretical predictions remain accurate for a variety of non-spherical geometries, including prolate and oblate spheroids and cones.

As discussed above, even weak advective effects can enhance the propulsion of the surfer when $\alpha > 0$. This observation naturally raises the question of whether such enhancement persists as Pe and Re increase beyond the asymptotically small regime, approaching $\mathscr{O}(1)$ and eventually reaching values much greater than one. Equally important is the behaviour of propulsion efficiency under these conditions: How does it vary with increasing Pe and Re? To address these questions, we extend our simulations to cover a broader range of parameters, specifically $Pe = 10^{-2}$, 10^{-1}, 10^{0}, 10^{1}, 10^{2}, and 10^{3} and $Re = 10^{-2}$, 10^{-1}, 10^{0}, 10^{1}, 10^{2}, and 10^{3}. These values represent the nominal Pe and Re as defined in (2.3). The effective values (Pe_e and Re_e), however, differ as they depend on the actual propulsion speed determined from the simulations, with $Pe_e = Pe\,\mathscr{U}$ and $Re_e = Re\,\mathscr{U}$.

Figure 3 presents the simulation results for spherical surfers with $d/R = 1/2$, 1, and 3/2 (from top to bottom). Each row shows contour plots of the normalised propulsion speed $\mathscr{U}$ (left) and the normalised fuel efficiency $\mathscr{E}$ (right) as functions of the Péclet and Reynolds numbers. The normalised fuel efficiency is defined as

$$\mathscr{E} = \frac{\underset{\sim}{U}/Sh}{U^\star/Sh^\star} = \frac{\mathscr{U}}{Sh/Sh^\star}, \tag{4.2}$$

https://doi.org/10.1017/jfm.2025.11027 Published online by Cambridge University Press

where Sh is the dimensionless release rate and $Sh^\star$ denotes its value in the limit where the transport of the released agent is purely diffusive, see also (2.24). This ratio serves as a measure of propulsion efficiency, quantifying how effectively the chemical energy released through surface-tension gradients is utilised to overcome viscous drag and sustain motion. We note that alternative efficiency metrics (e.g. cost of transport) could also be adopted, depending on the physical interpretation of the solute-release mechanism and the specific performance criterion of interest. While these contour maps provide a global view of propulsion performance across the Pe–Re parameter space, it is also instructive to examine systematic variations along one parameter at a time. To this end, figure 3 is complemented by figures 4–6, which show detailed trends of $\mathscr{U}$ and Sh along fixed-Pe and fixed-Re slices for the three release configurations ($d/R = 1/2$, 1 and $3/2$).

From these figures, we observe that, across all configurations, both the normalised propulsion speed $\mathscr{U}$ and the fuel efficiency $\mathscr{E}$ initially increase with Pe and Re, attain a peak and then decline as advective transport becomes dominant over diffusion. This non-monotonic behaviour reveals the existence of optimal (Pe, Re) combinations for each surfer, at which propulsion speed and efficiency are maximised. Although the peaks in $\mathscr{U}$ and $\mathscr{E}$ occur at slightly different values, they consistently appear around $Pe \sim Re \sim \mathscr{O}(1)$. As previously discussed in connection with table 1, the numerical results in the small-Pe, small-Re regime closely follow the theoretical prediction of (4.1) – see the dashed lines in the top rows of figures 4–6 – thereby confirming the validity of the asymptotic analysis. As either parameter increases, deviations from the asymptotic law become evident, with the propulsion speed ultimately reaching a maximum before decreasing at larger Pe and Re. We note that while increasing the density of numerical data points in the vicinity of $Pe \sim Re \sim \mathscr{O}(1)$ would further sharpen the curves, any resulting adjustments to the location or magnitude of the maxima are expected to be minimal.

At sufficiently large Pe and Re, both $\mathscr{U}$ and $\mathscr{E}$ exhibit pronounced decay. Examination of the contour and line plots reveals that the reduction with Re – approximately following a $Re^{-2/5}$ trend (see top-right panels in figures 4–6) – is much steeper than that with Pe, indicating that inertial effects are more detrimental to propulsion performance than the convective depletion of the active agent. Specifically, increasing Pe at fixed Re leads to a gradual decrease in $\mathscr{U}$ and $\mathscr{E}$, whereas increasing Re at fixed Pe produces a much sharper drop. This overall behaviour qualitatively resembles that of autophoretic Janus particles with negative mobility coefficients, where the propulsion speed rises with Pe, peaks, and subsequently declines at large Pe (Michelin & Lauga 2014). However, it differs from that of pusher-type squirmers, whose speeds increase with Re and eventually plateau instead of decreasing (Chisholm *et al.* 2016).

The bottom rows of figures 4–6 show the behaviour of the normalised Sherwood number, $Sh/Sh^\star$. These results indicate that the dependence of $Sh/Sh^\star$ on Re is relatively weak across all configurations, whereas its variation with Pe is much more pronounced. When $Sh/Sh^\star$ is replotted against the effective Péclet number (see insets), the data corresponding to different Re values nearly collapse onto a single master curve. At large Pe_e, the results approach a $Pe_e^{1/3}$ scaling, in agreement with classical asymptotic predictions for convective mass transfer at low and moderate Reynolds numbers (see, e.g. Acrivos & Goddard 1965; Leal 2007). Although less apparent in the insets, it is worth recalling that, in the opposite limit of small Pe, the normalised Sherwood number scales linearly with Pe at leading order, as predicted by (2.23).

A practical example of how our findings can inform surfer design is the selection of an optimal surfer size. In the Stokes regime, it has been shown that the propulsion speed, for a given discharged active agent and release configuration, is independent of

https://doi.org/10.1017/jfm.2025.11027 Published online by Cambridge University Press

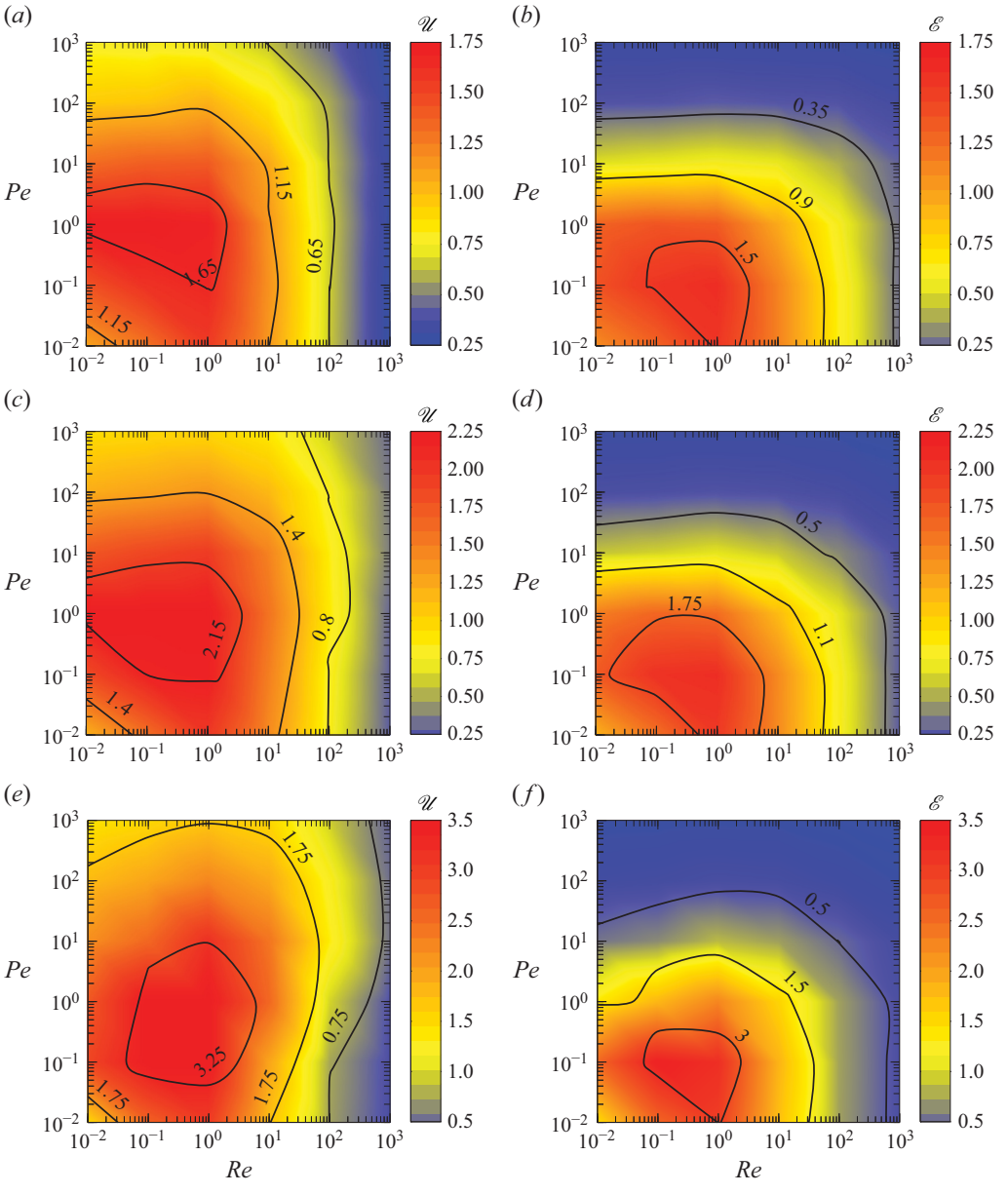


Figure 3. Contour plots of the normalised propulsion speed (a,c,e) and fuel efficiency (b,d,f) for a spherical surfer with $d = R/2$ (a,b), $d = R$ (c,d) and $d = 3R/2$ (e,f).

the surfer's characteristic size (Lauga & Davis 2012; Masoud & Stone 2014). In this limit, both the Marangoni-driven surface-tension force and the opposing hydrodynamic drag scale linearly with size, resulting in a size-independent propulsion velocity. As the surfer becomes larger, however, the associated Péclet and Reynolds numbers also rise, and, according to our results, there exists a narrow range of sizes corresponding to $Pe \sim Re \sim \mathcal{O}(1)$ that deliver optimal propulsion performance. Beyond this regime, further increases in size lead to a deterioration of both propulsion speed and fuel efficiency, as hydrodynamic resistance (roughly scaling quadratically with speed) and the rate of mass

https://doi.org/10.1017/jfm.2025.11027 Published online by Cambridge University Press

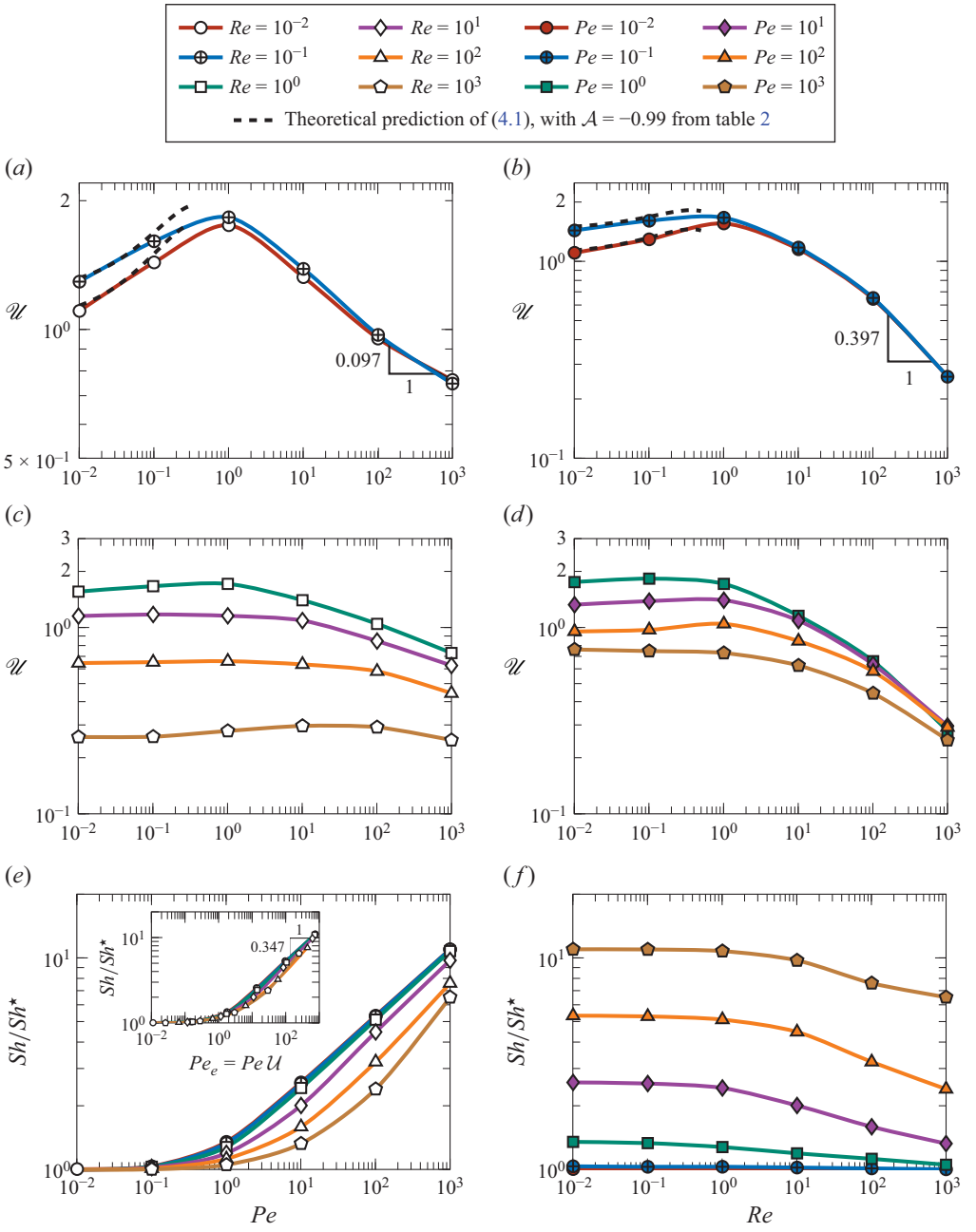


Figure 4. Normalised propulsion speed (first two rows) and Sherwood number (last row) of a spherical surfer with $d = R/2$ as a function of the Péclet number (a,c,e, open symbols) and Reynolds number (b,d,f, filled symbols), at fixed values of Re and Pe, respectively. Both parameters are varied from 10^{-2} to 10^{3} in decade increments on a logarithmic scale. In the first row, black dashed lines indicate the theoretical predictions of (4.1), valid in the limit of small Péclet and Reynolds numbers. The solid curves correspond to contour slices from the top row of figure 3. The inset in panel (e) shows the dependence of $Sh/Sh^{\star}$ on the effective Péclet number defined as $Pe_e = Pe\,\mathscr{U}$.

https://doi.org/10.1017/jfm.2025.11027 Published online by Cambridge University Press

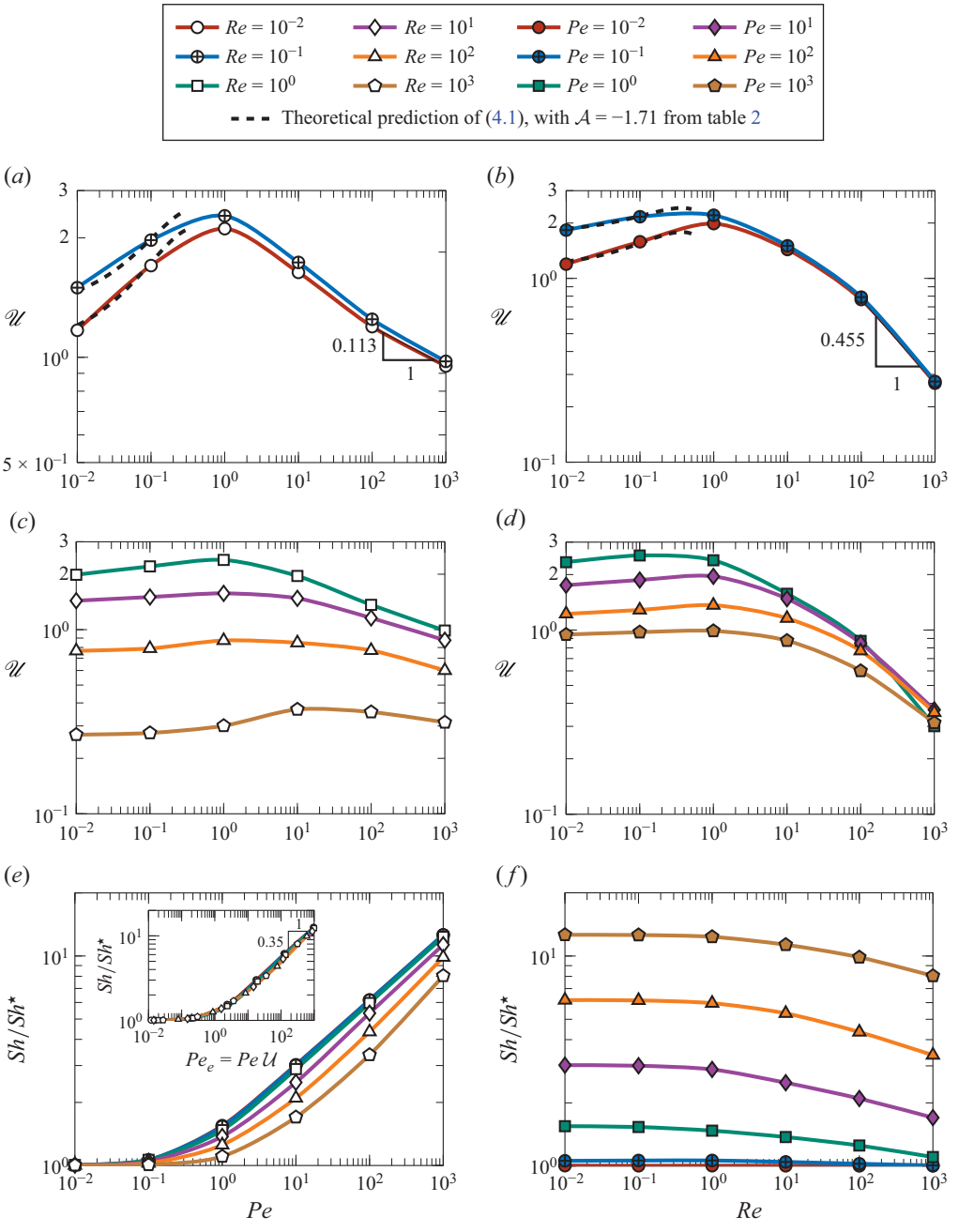


Figure 5. Normalised propulsion speed (first two rows) and Sherwood number (last row) of a spherical surfer with $d = R$ as a function of the Péclet number (a,c,e, open symbols) and Reynolds number (b,d,f, filled symbols), at fixed values of Re and Pe, respectively. Both parameters are varied from 10^{-2} to 10^{3} in decade increments on a logarithmic scale. In the first row, black dashed lines indicate the theoretical predictions of (4.1), valid in the limit of small Péclet and Reynolds numbers. The solid curves correspond to contour slices from the middle row of figure 3. The inset in panel (e) shows the dependence of $Sh/Sh^{\star}$ on the effective Péclet number defined as $Pe_e = Pe\,\mathscr{U}$.

https://doi.org/10.1017/jfm.2025.11027 Published online by Cambridge University Press

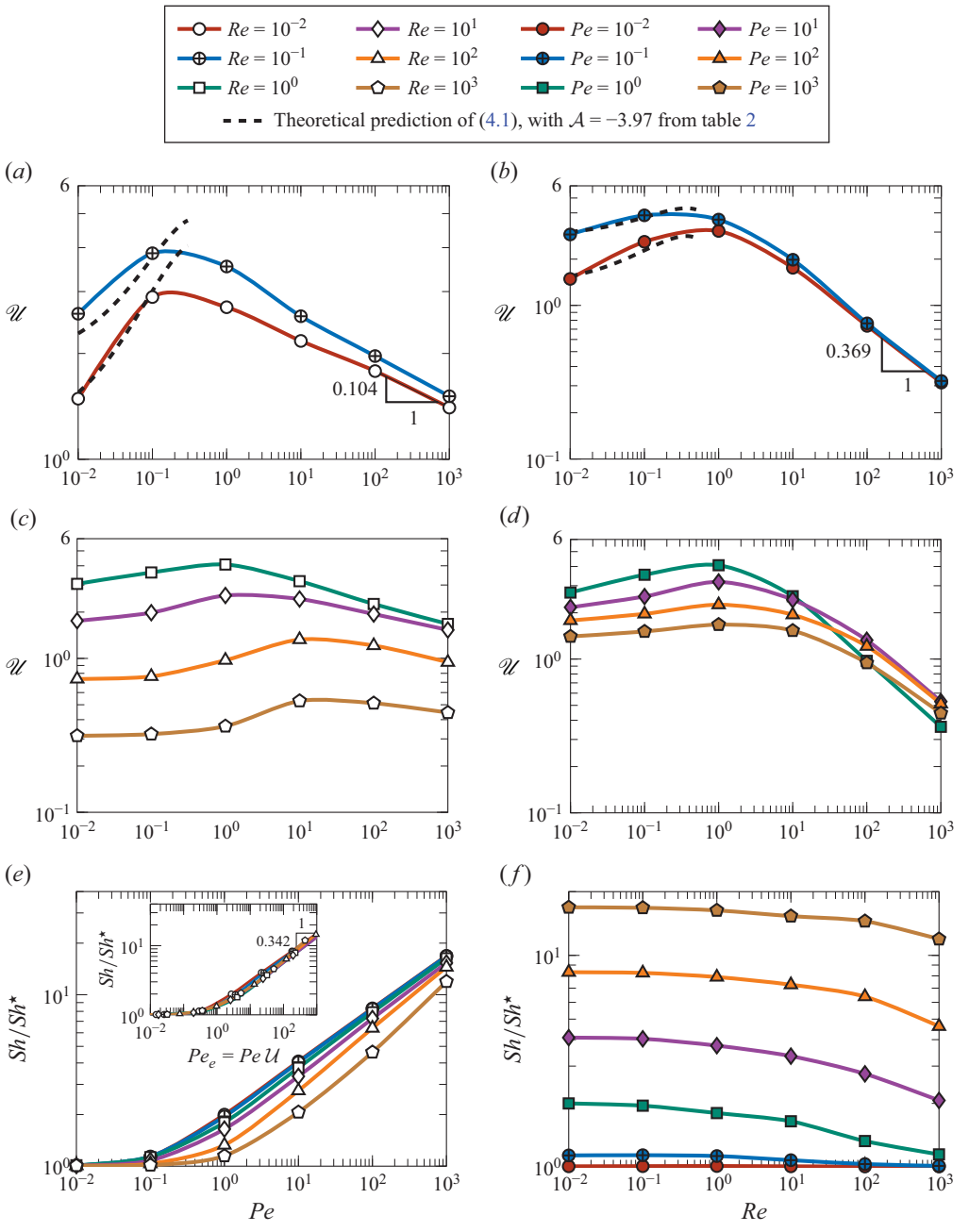


Figure 6. Normalised propulsion speed (first two rows) and Sherwood number (last row) of a spherical surfer with $d = 3R/2$ as a function of the Péclet number (a,c,e, open symbols) and Reynolds number (b,d,f, filled symbols), at fixed values of Re and Pe, respectively. Both parameters are varied from 10^{-2} to 10^3 in decade increments on a logarithmic scale. In the first row, black dashed lines indicate the theoretical predictions of (4.1), valid in the limit of small Péclet and Reynolds numbers. The solid curves correspond to contour slices from the bottom row of figure 3. The inset in panel (e) shows the dependence of $Sh/Sh^\star$ on the effective Péclet number defined as $Pe_e = Pe\,\mathscr{U}$.

https://doi.org/10.1017/jfm.2025.11027 Published online by Cambridge University Press

β	$d/R = 1 - \cos\beta$	$\mathbb{U}^\star = \dfrac{\mu\, U^\star}{\alpha\, c_s}$	$Sh^\star = \dfrac{\dot{m}^\star}{2\pi\, \mathscr{D}\, \ell\, c_s}$	$\mathscr{A} = -\dfrac{Sh^\star}{16\mathbb{U}^\star}$
$\pi/6$	$1 - \sqrt{3}/2$	0.021	0.22	−0.67
$\pi/3$	$1/2$	0.031	0.49	−0.99
$\pi/2$	1	0.027	0.74	−1.71
$2\pi/3$	$3/2$	0.014	0.91	−3.97
$5\pi/6$	$1 + \sqrt{3}/2$	0.003	0.99	−20.55

Table 2. The dimensionless propulsion speed ($\mathbb{U}^\star$), Sherwood number ($Sh^\star$) and multiplier $\mathscr{A}$ for the model surfer considered in numerical simulations for several agent release configurations (see figure 2*a*), all evaluated at $Pe = Re = 0$.

transfer intensify, while the surface-tension force continues to grow only approximately linearly with size. Nevertheless, the advective boost attainable through moderate size increase can lead to several-fold enhancements in both speed and efficiency, depending on the details of the release configuration.

Another key design consideration is the release configuration itself, characterised in the model surfer by the width of the active region, d. Table 2 summarises the dimensionless propulsion speed $\mathbb{U}^\star$, Sherwood number $Sh^\star$ and multiplier $\mathscr{A}$ for several d/R values in the limit of $Pe = Re = 0$. In the absence of advection, the propulsion speed increases with d/R up to a maximum near $d/R = 1/2$, beyond which it decreases as the active region widens further. In contrast, the dimensionless fuel efficiency, quantified by $\mathbb{U}^\star/Sh^\star$, decreases monotonically with increasing d/R. For example, when d/R increases from $1/2$ to $3/2$, the propulsion speed is reduced by roughly a factor of two, while the corresponding fuel efficiency drops by approximately fourfold. At finite Pe and Re, however, the situation changes: when evaluated at their respective optimal conditions, surfers with $d/R = 1/2$ and $d/R = 3/2$ attain comparable maximum propulsion speeds. Despite its lower baseline value of $\mathbb{U}^\star$, the surfer with the wider active region ($d/R = 3/2$) benefits from stronger advective enhancement at moderate Pe and Re (compare the top rows of figures 4 and 6), allowing it to reach peak speeds similar to those of the more localised release configuration. A difference in fuel efficiency nevertheless persists: even at optimal conditions, the surfer with $d/R = 3/2$ remains approximately a factor of two less fuel efficient than its $d/R = 1/2$ counterpart. These results demonstrate how variations in the release configuration, by modulating both the initial surface-tension distribution and the advective response, can significantly impact the propulsion speed and energetic cost of Marangoni surfing.

As a final remark on propulsion performance, we briefly comment on the less practical case of $\alpha < 0$, where the release of the active agent locally increases surface tension. Simulation results for the representative configuration corresponding to $d/R = 1/2$ (not shown for brevity) indicate that advective effects lead to a reduction in the normalised propulsion speed as Pe and Re increase. This trend is qualitatively similar to that observed for autophoretic Janus particles with positive mobility coefficients, where advection progressively degrades propulsion at high Pe (Michelin & Lauga 2014). Likewise, puller-type squirmers experience a decline in the normalised speed with increasing Re, although they may also undergo instabilities and symmetry breaking at sufficiently large Reynolds numbers (Chisholm *et al.* 2016). Our simulations further suggest that, at sufficiently large Pe, the direction of propulsion may reverse (i.e. the normalised speed becomes negative). However, without a detailed stability analysis, it remains unclear whether steady

https://doi.org/10.1017/jfm.2025.11027 Published online by Cambridge University Press

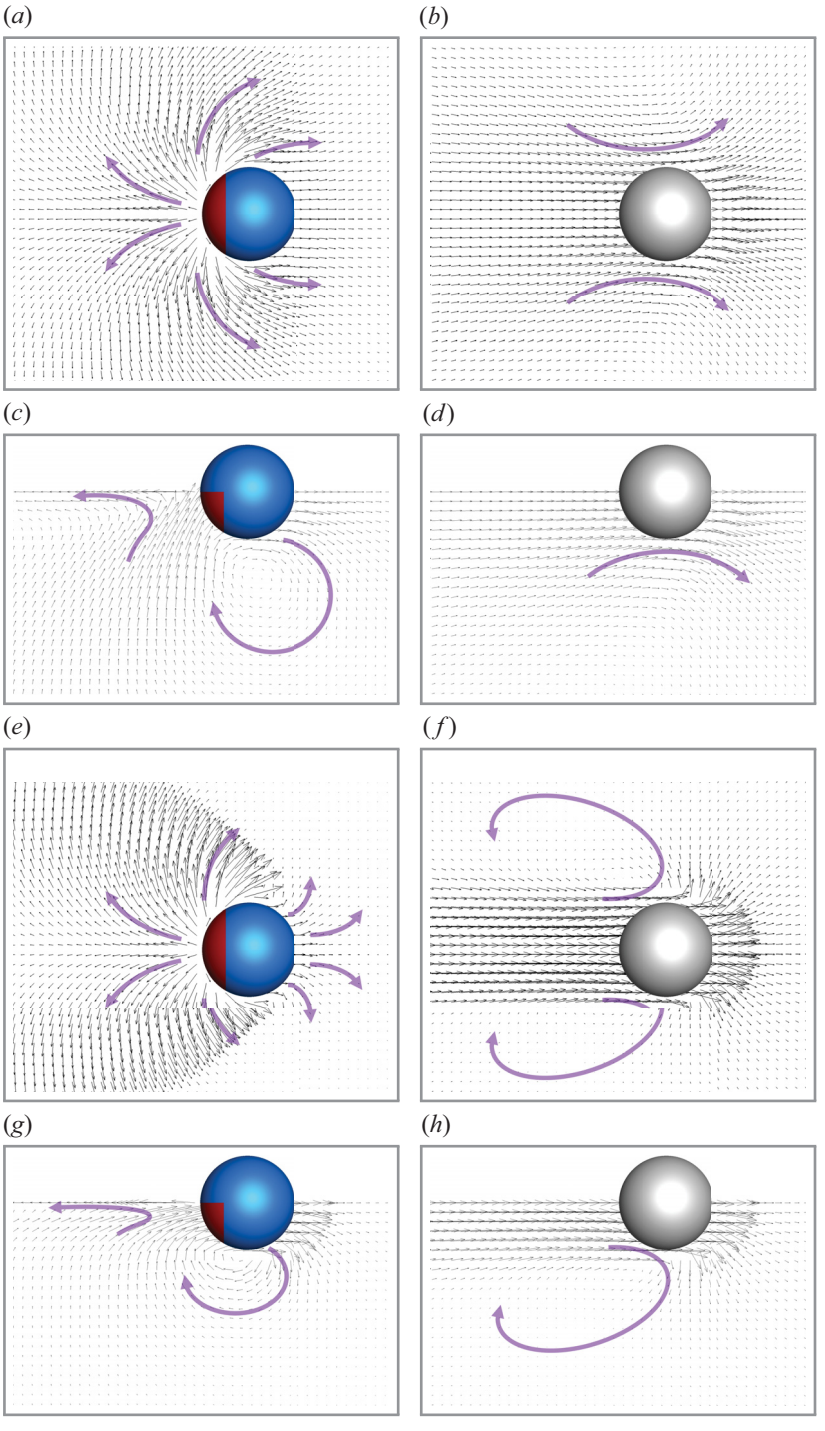


Figure 7. Flow field plots comparing the motion of an active, Marangoni-driven spherical surfer with positive α and $d = R/2$ at $Pe = 10$ (a,c,e,g) with that of a passive sphere translating without Marangoni stresses present at the interface (b,d,f,h), both at $Re = 1$ (top two rows) and $Re = 10^2$ (bottom two rows). The first and third rows show the surface flow at the interface, while the second and fourth rows depict the velocity fields in the x –z plane that bisects the surfer. Thick purple arrows indicate the overall flow direction and black velocity vectors are scaled independently in each panel to aid visualisation. The direction of propulsion is from left to right.

https://doi.org/10.1017/jfm.2025.11027 Published online by Cambridge University Press

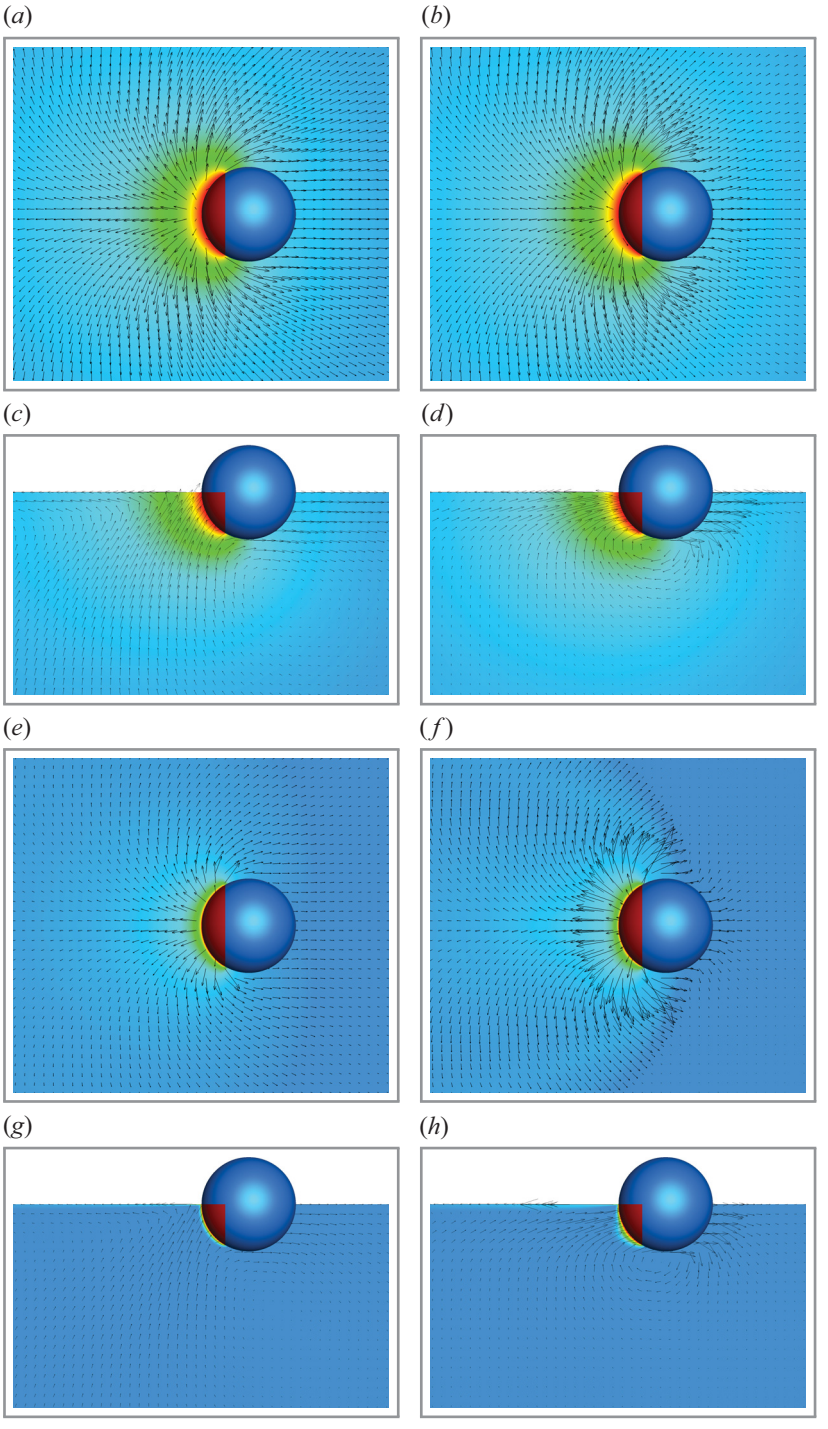


Figure 8. Velocity fields and concentration contours at the interface (first and third rows) and in the x–z plane bisecting the surfer (second and fourth rows), corresponding to the Marangoni-driven motion of an active sphere with positive α and $d = R/2$ at $Re = 1$ (a,c,e,g) and $Re = 10^2$ (b,d,f,h). The top two and bottom two rows show the results for $Pe = 10^{-1}$ and $Pe = 10^3$, respectively. In the concentration maps, the highest concentration appears at the active region of the surfer (coloured red), while the lowest is observed in the far field (coloured blue).

https://doi.org/10.1017/jfm.2025.11027 Published online by Cambridge University Press

propulsion could be sustained under these conditions. Additionally, interface deformation may no longer be negligible under such conditions.

To conclude our discussion of the propulsion behaviour of the surfers, we present selected examples of the fluid flow field and concentration distribution around a surfer with $d/R = 1/2$. Specifically, results are shown for $Pe = 10^{-1}$, 10 and 10^3 and $Re = 1$ and 10^2 (see figures 7 and 8). As expected, the discharge of the active agent propels the surfer and induces a radial dilation of the interface from a stagnation point located near the release site (see figures 7*a* and 7*e*). This point coincides with the region of minimum interfacial tension (see the first and third rows of figure 8). The combination of the surfer's motion and interfacial dilation gives rise to a flow pattern beneath the surface that resembles a deformed vortex ring. This vortex originates from the bulk recirculation required to maintain incompressibility. When viewed in the x–z plane bisecting the surfer, the three-dimensional swirling flow appears as a pair of counter-rotating vortices: one located beneath the surfer and the other just upstream of the stagnation point (see figures 7*c* and 7*g*, and the second and fourth rows of figure 8). This flow topology is a hallmark of Marangoni propulsion and contrasts sharply with the flow generated by the motion of an inert particle at the interface (compare figures 7*a* and 7*e* with figures 7*b* and 7*f*). In particular, figure 7(*d*) demonstrates that, at low Re, no vortex forms beneath the free surface or behind the inert particle. Lastly, comparing the top and bottom two rows of figure 8, we see that the overall flow structure near the surfer remains qualitatively similar across the examined range of Pe. However, subtle differences emerge at high Re, particularly in the size and orientation of the vortical structures (see figures 8*b* and 8*f*).

5. Summary

We developed a comprehensive theoretical and computational framework to study the Marangoni-driven propulsion of active surfers at liquid–gas interfaces in the presence of advective mass and momentum transport. By applying the reciprocal theorem and singular perturbation expansions, we derived a general asymptotic formula that captures the leading-order corrections to the propulsion speed in the limit of small Péclet and Reynolds numbers. Crucially, this formula is broadly applicable to purely translating surfers, independent of their shape, the agent discharge mechanism or the specific release configuration. Our analysis reveals that, unlike bulk microswimmers, the normalised propulsion speed of Marangoni surfers exhibits logarithmic sensitivity to both Péclet and Reynolds numbers at leading order, indicating a stronger-than-expected influence of advective effects even at small parameter values. Furthermore, the prefactor appearing in the asymptotic expression offers explicit guidance for optimising surfer design through adjustments in geometry and agent release strategies.

Complementing our theoretical findings, we conducted detailed numerical simulations for a representative spherical surfer across a wide range of Péclet and Reynolds numbers. The simulation results confirmed the theoretical predictions for $Pe \ll 1$ and $Re \ll 1$, and further mapped the propulsion speed and fuel efficiency across broader parameter spaces. Notably, we identified the existence of optimal Péclet and Reynolds numbers (typically around order one) that maximise propulsion performance. Beyond these optimal points, increasing advective mass transport or inertial effects leads to a deterioration in both speed and efficiency, with the decline being more pronounced with the Reynolds number. Additionally, we demonstrated that both the surfer's size and the configuration of the active region critically influence performance at various Péclet and Reynolds numbers, offering practical strategies for the design of future Marangoni surfers.

https://doi.org/10.1017/jfm.2025.11027 Published online by Cambridge University Press

In the future, it would be worthwhile to extend the present analysis to include the rotational motion of surfers – a mode of locomotion reported by Sur *et al.* (2019) under certain conditions and at sufficiently large advective effects – to provide a more complete understanding of propulsion dynamics at high *Pe* and *Re*.

Overall, our findings advance the current understanding of the interplay between convective transport – of both mass and momentum – and Marangoni propulsion at fluid interfaces. By establishing a general theoretical framework applicable to a broad range of surfer geometries and agent release mechanisms, our study provides a solid basis for the design of next-generation miniature surfing robots. Such robots, whether operating individually or in coordinated fleets, offer promising capabilities for applications including environmental sensing, microfluidic manipulation and autonomous surface exploration.

Acknowledgements. Financial support from the National Science Foundation under Grant Nos. CBET-2449852 and CBET-2449625 (H.M.), and CBET-2423497 (J.P.R.) is acknowledged. The use of AI for language editing and improving the manuscript's readability is also acknowledged.

Declaration of interests. The authors declare no conflict of interest.

References

Acrivos, A. & Goddard, J.D. 1965 Asymptotic expansions for laminar forced-convection heat and mass transfer. *J. Fluid Mech.* **23** (2), 273–291.

Andersen, N.M. 1976 A comparative study of locomotion on the water surface in semiaquatic bugs (Insecta, Hemiptera, Gerromorpha). *Vidensk. Meddr. Dansk. Naturhist. Foren.* **139**, 337–396.

Angelini, T.E., Roper, M., Kolter, R., Weitz, D.A. & Brenner, M.P. 2009 Bacillus subtilis spreads by surfing on waves of surfactant. *Proc. Natl Acad. Sci.* **106** (43), 18109–18113.

Baddour, N. 2011 Two-dimensional Fourier transforms in polar coordinates. In *Advances in Imaging and Electron Physics* (ed. P.W. Hawkes), vol. 165, pp. 1–45. Elsevier.

Bánsági Jr, T., Wrobel, M.M., Scott, S.K. & Taylor, A.F. 2013 Motion and interaction of aspirin crystals at aqueous–air interfaces. *J. Phys. Chem. B* **117** (43), 13572–13577.

Bassik, N., Abebe, B.T. & Gracias, D.H. 2008 Solvent driven motion of lithographically fabricated gels. *Langmuir* **24** (21), 12158–12163.

Basualdo, F.N.P., Bolopion, A., Gauthier, M. & Lambert, P. 2021 A microrobotic platform actuated by thermocapillary flows for manipulation at the air-water interface. *Sci. Robot.* **6** (52), eabd3557.

Bechard, S., Timm, M.L., Masoud, H. & Rothstein, J.P. 2023 Using footpad sculpturing to enhance the maneuverability and speed of a robotic Marangoni surfer. *Biomimetics* **8** (5), 440.

Boniface, D., Cottin-Bizonne, C., Detcheverry, F. & Ybert, C. 2021 Role of Marangoni forces in the velocity of symmetric interfacial swimmers. *Phys. Rev. Fluids* **6** (10), 104006.

Boniface, D., Cottin-Bizonne, C., Kervil, R., Ybert, C. & Detcheverry, F. 2019 Self-propulsion of symmetric chemically active particles: point-source model and experiments on camphor disks. *Phys. Rev. E* **99** (6), 062605.

Brenner, H. 1963 Forced convection heat and mass transfer at small Péclet numbers from a particle of arbitrary shape. *Chem. Engng Sci.* **18** (2), 109–122.

Brenner, H. & Cox, R.G. 1963 The resistance to a particle of arbitrary shape in translational motion at small Reynolds numbers. *J. Fluid Mech.* **17** (4), 561–595.

Burton, L.J., Cheng, N. & Bush, J.W. 2014 The cocktail boat. *Integr. Compar. Biol.* **54** (5), 969–973.

Bush, J.W.M. & Hu, D.L. 2006 Walking on water: biolocomotion at the interface. *Annu. Rev. Fluid Mech.* **38**, 339–369.

Bush, J.W.M., Hu, D.L. & Prakash, M. 2007 The integument of water-walking arthropods: form and function. *Adv. Insect Physiol.* **34**, 117–192.

Chisholm, N.G., Legendre, D., Lauga, E. & Khair, A.S. 2016 A squirmer across Reynolds numbers. *J. Fluid Mech.* **796**, 233–256.

Crowdy, D. 2020 Collective viscous propulsion of a two-dimensional flotilla of Marangoni boats. *Phys. Rev. Fluids* **5** (12), 124004.

Crowdy, D. 2021 Viscous propulsion of a two-dimensional Marangoni boat driven by reaction and diffusion of insoluble surfactant. *Phys. Rev. Fluids* **6** (6), 064003.

Daniels, R., *et al.* 2006 Quorum signal molecules as biosurfactants affecting swarming in Rhizobium etli. *Proc. Natl Acad. Sci. USA* **103** (40), 14965–14970.

https://doi.org/10.1017/jfm.2025.11027 Published online by Cambridge University Press

DEHDASHTI, E. & MASOUD, H. 2020 Forced convection heat transfer from a particle at small and large Péclet numbers. *J. Heat Transfer* **142** (6), 061803.

DIETRICH, K., JAENSSON, N., BUTTINONI, I., VOLPE, G. & ISA, L. 2020 Microscale Marangoni surfers. *Phys. Rev. Lett.* **125** (9), 098001.

DOMÍNGUEZ, A. & POPESCU, M.N. 2018 Phase coexistence in a monolayer of active particles induced by Marangoni flows. *Soft Matt.* **14** (39), 8017–8029.

ENDER, H. & KIERFELD, J. 2021 From diffusive mass transfer in Stokes flow to low Reynolds number Marangoni boats. *Eur. Phys. J. E* **44**, 1–25.

FAUVART, M., PHILLIPS, P., BACHASPATIMAYUM, D., VERSTRAETEN, N., FRANSAER, J., MICHIELS, J. & VERMANT, J. 2012 Surface tension gradient control of bacterial swarming in colonies of Pseudomonas aeruginosa. *Soft Matt.* **8** (1), 70–76.

FRENKEL, M., MULTANEN, V., GRYNYOV, R., MUSIN, A., BORMASHENKO, Y. & BORMASHENKO, E. 2017 Camphor-engine-driven micro-boat guides evolution of chemical gardens. *Sci. Rep.* **7** (1), 3930.

GIDITURI, H., PANCHAGNULA, M.V. & POTOTSKY, A. 2019 Dynamics of a fully wetted Marangoni surfer at the fluid-fluid interface. *Soft Matt.* **15** (10), 2284–2291.

GIROT, A., DANNE, N., WÜRGER, A., BICKEL, T., REN, F., LOUDET, J. & POULIGNY, B. 2016 Motion of optically heated spheres at the water–air interface. *Langmuir* **32** (11), 2687–2697.

GRADSHTEYN, I.S. & RYZHIK, I.M. 2007 *Table of Integrals, Series, and Products*. Academic Press.

HARSHEY, R.M. 2003 Bacterial motility on a surface: many ways to a common goal. *Annu. Rev. Microbiol.* **57** (1), 249–273.

HINCH, E.J. 1991 *Perturbation Methods*. Cambridge University Press.

IVANOV, D. & NIKOLOV, S. 2019 Molecular engine boat. *Phys. Educ.* **54** (4), 045006.

JAFARI KANG, S., SUR, S., ROTHSTEIN, J.P. & MASOUD, H. 2020 Forward, reverse, and no motion of Marangoni surfers under confinement. *Phys. Rev. Fluids* **5** (8), 084004.

JIN, H., MARMUR, A., IKKALA, O. & RAS, R.H. 2012 Vapour-driven Marangoni propulsion: continuous, prolonged and tunable motion. *Chem. Sci.* **3** (8), 2526–2529.

KAPLUN, S. 1957 Low Reynolds number flow past a circular cylinder. *J. Math. Mech.* **6** (5), 595–603.

KAPLUN, S. & LAGERSTROM, P.A. 1957 Asymptotic expansions of Navier–Stokes solutions for small Reynolds numbers. *J. Math. Mech.* **6** (5), 585–593.

KEARNS, D.B. 2010 A field guide to bacterial swarming motility. *Nat. Rev. Microbiol.* **8** (9), 634–644.

KITAHATA, H., HIROMATSU, S.-I., DOI, Y., NAKATA, S. & RAFIQUL ISLAM, M. 2004 Self-motion of a camphor disk coupled with convection. *Phys. Chem. Chem. Phys.* **6** (9), 2409–2414.

KOYANO, Y., GRYCIUK, M., SKROBANSKA, P., MALECKI, M., SUMINO, Y., KITAHATA, H. & GORECKI, J. 2017 Relationship between the size of a camphor-driven rotor and its angular velocity. *Phys. Rev. E* **96** (1), 012609.

KWAK, B. & BAE, J. 2017 Skimming and steering of a non-tethered miniature robot on the water surface using Marangoni propulsion. In *2017 IEEE/RSJ International Conference on Intelligent Robots and Systems (IROS)*, pp. 3217–3222. IEEE.

KWAK, B., CHOI, S. & BAE, J. 2020 Directional motion on water surface with keel extruded footpads propelled by Marangoni effect. *IEEE Robot. Autom. Lett.* **5** (4), 6829–6836.

KWAK, B., CHOI, S., MAENG, J. & BAE, J. 2021 Marangoni effect inspired robotic self-propulsion over a water surface using a flow-imbibition-powered microfluidic pump. *Sci. Rep.* **11** (1), 1–13.

LAGERSTROM, P.A. & COLE, J.D. 1955 Examples illustrating expansion procedures for the Navier–Stokes equations. *J. Rat. Mech. Anal.* **4**, 817–882.

LAMB, H. 1932 *Hydrodynamics*. Cambridge University Press.

LANG, C., SEIFERT, K. & DETTNER, K. 2012 Skimming behaviour and spreading potential of Stenus species and Dianous coerulescens (Coleoptera: Staphylinidae). *Naturwissenschaften* **99** (11), 937–947.

LAUGA, E. & DAVIS, A.M.J. 2012 Viscous Marangoni propulsion. *J. Fluid Mech.* **705**, 120–133.

LEAL, L.G. 2007 *Advanced Transport Phenomena: Fluid Mechanics and Convective Transport Processes*. Cambridge University Press.

LI, H., QIAO, L., LIU, X. & LUO, C. 2012 Fabrication and testing of a self-propelled, miniaturized PDMS flotilla. *Microsyst. Technol.* **18** (9–10), 1431–1444.

LIAKOS, I.L., SALVAGNINI, P., SCARPELLINI, A., CARZINO, R., BELTRAN, C., MELE, E., MURINO, V. & ATHANASSIOU, A. 2016 Biomimetic locomotion on water of a porous natural polymeric composite. *Adv. Mater. Interfaces* **3** (11), 1500854.

LINSENMAIR, K.E. & JANDER, R. 1963 Das 'entspannungsschwimmen' von velia und stenus. *Naturwissenschaften* **50** (6), 231–231.

LÖFFLER, R.J.G., HANCZYC, M.M. & GORECKI, J. 2019 A hybrid camphor-camphene wax material for studies on self-propelled motion. *Phys. Chem. Chem. Phys.* **21** (45), 24852–24856.

https://doi.org/10.1017/jfm.2025.11027 Published online by Cambridge University Press

LOVALENTI, P.M. & BRADY, J.F. 1993 The hydrodynamic force on a rigid particle undergoing arbitrary time-dependent motion at small Reynolds number. *J. Fluid Mech.* **256**, 561–605.
LUO, C., LI, H., QIAO, L. & LIU, X. 2012 Development of surface tension-driven microboats and microflotillas. *Microsyst. Technol.* **18** (9–10), 1525–1541.
MAGGI, C., SAGLIMBENI, F., DIPALO, M., DE ANGELIS, F. & DI LEONARDO, R. 2015 Micromotors with asymmetric shape that efficiently convert light into work by thermocapillary effects. *Nat. Commun.* **6**, 7855.
MALGARETTI, P., POPESCU, M.N. & DIETRICH, S. 2016 Active colloids at fluid interfaces. *Soft Matt.* **12**, 4007–4023.
MASOUD, H. & ROTHSTEIN, J.P. 2022 Diffusive mass transfer from a Janus sphere. *Phys. Rev. Fluids* **7** (7), 070501.
MASOUD, H. & SHELLEY, M.J. 2014 Collective surfing of chemically active particles. *Phys. Rev. Lett.* **112** (12), 128304.
MASOUD, H. & STONE, H.A. 2014 A reciprocal theorem for Marangoni propulsion. *J. Fluid Mech.* **741**, R4.
MASOUD, H. & STONE, H.A. 2019 The reciprocal theorem in fluid dynamics and transport phenomena. *J. Fluid Mech.* **879**, P1.
MICHELIN, S. & LAUGA, E. 2014 Phoretic self-propulsion at finite Péclet numbers. *J. Fluid Mech.* **747**, 572–604.
MOROHASHI, H., IMAI, M. & TOYOTA, T. 2019 Construction of a chemical motor-movable frame assembly based on camphor grains using water-floating 3D-printed models. *Chem. Phys. Lett.* **721**, 104–110.
MUSIN, A., GRYNYOV, R., FRENKEL, M. & BORMASHENKO, E. 2016 Self-propulsion of a metallic superoleophobic micro-boat. *J. Colloid Interface Sci.* **479**, 182–188.
NAGAYAMA, M., NAKATA, S., DOI, Y. & HAYASHIMA, Y. 2004 A theoretical and experimental study on the unidirectional motion of a camphor disk. *Physica D* **194** (3), 151–165.
NAKATA, S. & MURAKAMI, M. 2010 Self-motion of a camphor disk on an aqueous phase depending on the alkyl chain length of sulfate surfactants. *Langmuir* **26** (4), 2414–2417.
OOI, C.H., VAN NGUYEN, A., EVANS, G.M., GENDELMAN, O., BORMASHENKO, E. & NGUYEN, N. 2015 A floating self-propelling liquid marble containing aqueous ethanol solutions. *RSC Adv.* **5** (122), 101006–101012.
PENA-FRANCESCH, A., GILTINAN, J. & SITTI, M. 2019 Multifunctional and biodegradable self-propelled protein motors. *Nat. Commun.* **10** (1), 1–10.
PIMIENTA, V. & ANTOINE, C. 2014 Self-propulsion on liquid surfaces. *Curr. Opin. Colloid Interface Sci.* **19** (4), 290–299.
PROUDMAN, I. & PEARSON, J.R.A. 1957 Expansions at small Reynolds numbers for the flow past a sphere and a circular cylinder. *J. Fluid Mech.* **2** (3), 237–262.
QIAO, L., XIAO, D., LU, F.K. & LUO, C. 2012 Control of the radial motion of a self-propelled microboat through a side rudder. *Sensors Actuators A: Phys.* **188**, 359–366.
RENNEY, C., BREWER, A. & MOOIBROEK, T.J. 2013 Easy demonstration of the Marangoni effect by prolonged and directional motion: 'soap boat 2.0'. *J. Chem. Educ.* **90** (10), 1353–1357.
SATTERWHITE-WARDEN, J.E., KONDEPUDI, D.K., DIXON, J.A. & RUSLING, J.F. 2015 Co-operative motion of multiple benzoquinone disks at the air–water interface. *Phys. Chem. Chem. Phys.* **17** (44), 29891–29898.
SCHILDKNECHT, H. 1976 Chemical ecology–a chapter of modern natural products chemistry. *Angew. Chem. Intl Ed. Engl.* **15** (4), 214–222.
SHARMA, R., CHANG, S.T. & VELEV, O.D. 2012 Gel-based self-propelling particles get programmed to dance. *Langmuir* **28** (26), 10128–10135.
SHARMA, R., CORCORAN, T.E., GAROFF, S., PRZYBYCIEN, T.M. & TILTON, R.D. 2017 Transport of a partially wetted particle at the liquid/vapor interface under the influence of an externally imposed surfactant generated Marangoni stress. *Colloids Surf. A* **521**, 49–60.
SHIBUYA, Y. & MATSUSHITA, S. 2009 Electric current generation by camphor boats. *Mol. Cryst. Liq. Cryst.* **504** (1), 27–34.
SOH, S., BISHOP, K.J. & GRZYBOWSKI, B.A. 2008 Dynamic self-assembly in ensembles of camphor boats. *J. Phys. Chem. B* **112** (35), 10848–10853.
SOH, S., BRANICKI, M. & GRZYBOWSKI, B.A. 2011 Swarming in shallow waters. *J. Phys. Chem. Lett.* **2** (7), 770–774.
SRINIVASAN, A., ROCHE, J., RAVAINE, V. & KUHN, A. 2015 Synthesis of conducting asymmetric hydrogel particles showing autonomous motion. *Soft Matt.* **11** (20), 3958–3962.
SRIVASTAVA, S.K. & SCHMIDT, O.G. 2016 Autonomously propelled motors for value-added product synthesis and purification. *Chem. Eur. J.* **22** (27), 9072–9076.
SU, M. 2007 Liquid mixing driven motions of floating macroscopic objects. *Appl. Phys. Lett.* **90** (14), 144102.

https://doi.org/10.1017/jfm.2025.11027 Published online by Cambridge University Press

SUEMATSU, N.J., NAKATA, S., AWAZU, A. & NISHIMORI, H. 2010 Collective behavior of inanimate boats. *Phys. Rev. E* **81** (5), 056210.

SUR, S., MASOUD, H. & ROTHSTEIN, J.P. 2019 Translational and rotational motion of disk-shaped Marangoni surfers. *Phys. Fluids* **31** (10), 102101.

SUR, S., UVANOVIC, N., MASOUD, H. & ROTHSTEIN, J.P. 2021 The effect of shape on the motion and stability of Marangoni surfers. *J. Fluids Engng* **143** (1), 011301.

TIMM, M.L., JAFARI KANG, S., ROTHSTEIN, J.P. & MASOUD, H. 2021 A remotely controlled Marangoni surfer. *Bioinspir. Biomim.* **16** (6), 066014.

VAN DYKE, M.D. 1964 *Perturbation Methods in Fluid Dynamics*. Academic Press.

VANDADI, V., JAFARI KANG, S. & MASOUD, H. 2017 Reverse Marangoni surfing. *J. Fluid Mech.* **811**, 612–621.

WANG, L., YUAN, B., LU, J., TAN, S., LIU, F., YU, L., HE, Z. & LIU, J. 2016 Self-propelled and long-time transport motion of PVC particles on a water surface. *Adv. Mater.* **28** (21), 4065–4070.

WÜRGER, A. 2014 Thermally driven Marangoni surfers. *J. Fluid Mech.* **752**, 589–601.

XIAO, M., JIANG, C. & SHI, F. 2014 Design of a UV-responsive microactuator on a smart device for light-induced ON-OFF-ON motion. *NPG Asia Mater.* **6** (9), e128.

ZHANG, H., DUAN, W., LIU, L. & SEN, A. 2013 Depolymerization-powered autonomous motors using biocompatible fuel. *J. Am. Chem. Soc.* **135** (42), 15734–15737.

ZHANG, L., YUAN, Y., QIU, X., ZHANG, T., CHEN, Q. & HUANG, X. 2017 Marangoni effect-driven motion of miniature robots and generation of electricity on water. *Langmuir* **33** (44), 12609–12615.

ZHAO, G. & PUMERA, M. 2012 Liquid–liquid interface motion of a capsule motor powered by the interlayer Marangoni effect. *J. Phys. Chem. B* **116** (35), 10960–10963.

https://doi.org/10.1017/jfm.2025.11027 Published online by Cambridge University Press